JOURNAL OF MATERIALS RESEARCH AND TECHNOLOGY 2023;23:1252–1272

Available online at www.sciencedirect.com

jmr&t
Journal of Materials Research and Technology

journal homepage: www.elsevier.com/locate/jmrt

Original Article

Impact of processing defects on microstructure, surface quality, and tribological performance in 3D printed polymers

Nayan Dhakal [a,b,*], *Xiaolong Wang* [c], *Cayetano Espejo* [b], *Ardian Morina* [b], *Nazanin Emami* [a,**]

[a] *Polymer-tribology Group, Division of Machine Elements, Luleå University of Technology, SE 97187, Luleå, Sweden*
[b] *Institute of Functional Surfaces, School of Mechanical Engineering, University of Leeds, LS2 9JT, Leeds, United Kingdom*
[c] *State Key Laboratory of Solid Lubrication, Lanzhou Institute of Chemical Physics, CAS, Lanzhou, 730000, China*

ARTICLE INFO

Article history:
Received 3 October 2022
Accepted 13 January 2023
Available online 21 January 2023

Keywords:
3D printing
Tribology
Friction
Polymers
Porosity
Surface roughness

ABSTRACT

Additive manufacturing (AM), also known as three-dimensional (3D) printing, of polymer-based materials is growing as a time-efficient, economical, and environmentally sustainable technique for prototype development in load-bearing applications. This work investigates the defects arising from the processing in material extrusion-based AM of polymers and their impact on the part performance. The influence of raster angle orientation and printing speed on tribological characteristics, microstructure, and surface finish of acrylonitrile butadiene styrene (ABS) fabricated in a heated build chamber was studied. Comprehensive analysis with fractography and tomography revealed the formation, distribution, and locations of internal voids, while surface defects were studied with the topography analysis of as-printed surfaces. Surface roughness and tribological results show that printing speed can be optimally increased with a minimal impact on interlayer bonding and part performance. Increased printing speed allowed up to 58% effective reduction in printing time obtaining comparable mechanical properties at varying process parameters. 3D printed ABS exhibited dry sliding friction coefficients in the range of 0.18–0.23, whilst the maximum specific wear rate was 6.2×10^{-5} mm^3/Nm. Higher surface roughness and increased printing speed exhibited delayed running-in during dry sliding, while insignificant influence was observed for steady-state friction and wear behaviors. The findings indicate that improved surface finish and reduced internal defects can be achieved with a controlled build environment allowing for higher printing speed. The observations in this study are evidence that 3D printing can be adapted for the sustainable manufacturing of polymeric components for tribological applications.

---

[*] Corresponding author.
[**] Corresponding author.

E-mail addresses: nayan.dhakal@ltu.se (N. Dhakal), nazanin.emami@ltu.se (N. Emami).

https://doi.org/10.1016/j.jmrt.2023.01.086

1. Introduction

In recent years, three-dimensional (3D) printing of thermoplastics has garnered ample interest with a focus on developing new materials with improved efficiency, part properties, and higher processing speed. 3D printing offers substantial advantages over conventional subtractive manufacturing methods for polymer-based materials. The primary benefits of using 3D printing over conventional manufacturing are the higher design flexibility, customization of parts, and effective use of raw materials [1]. The inherent nature of layer-on-layer additive processing reduces resource-extensive and time-consuming design-manufacturing cycles allowing the production of lightweight components with reduced material wastage [2]. The efficient use of raw materials has added benefits in reducing production costs compared to conventional methods. However, sustainability in 3D printing is highly dependent on the employed technique, material selection, and the influence of processing parameters [3].

Fused filament fabrication (FFF) is an extrusion-based 3D printing technique with increasing popularity for the manufacturing of polymer-based materials. This is due to the ease of processing polymer materials, longer shelf-life of filaments, fabrication of complex geometries, effective mixing of fillers with polymer matrices, a wide range of fillers, reduced wastage, and easy recycling [4,5]. To date, the adoption of FFF technique for mass production of functional components is limited due to the anisotropic properties of finished products, limited resolution governed by the nozzle diameter, rough surface finish, and processing-dependent part quality. It is well known that FFF process parameters highly impact the quality and characteristics of printed parts resulting from the internal defects that originated during the processing, as observed in Refs. [6–8]. Certain parameters have a higher degree of influence and thus should be selected carefully, optimized, and adapted for efficient printing. However, fewer studies have been carried out to understand the influence of printing speed and raster angle orientation on surface quality and its direct consequences on tribological performance and mechanical properties compared to other process variables [9–11]. Most investigations on the properties of FFF-printed polymers have utilized acrylonitrile butadiene styrene (ABS) materials owing to their low melting point (about 200 °C) and ease of printing. ABS materials are well suited for printing because of their lightweight, chemically inert, eco-friendly, and reusable characteristics [10]. Such features help to investigate the influence of process parameters on part characteristics and printability to establish an effective methodology for high-quality printing [12–14].

It should be noted that rough surface finish and porosity are two of the most important challenges with FFF 3D printing. Buj-Corral et al. [15] investigated the impact of FFF processing parameters on dimensional accuracy, surface roughness, and porosity. Authors suggested that print speed and layer height affects the porosity, while surface roughness depends on the layer height. A layer height of 0.25 mm was suggested for higher dimensional accuracy, while 0.05 mm layer height provided lower surface roughness. However, this is not optimal as lower layer height results in longer built time which is often undesirable. Krolczyk et al. [16] earlier compared the surface roughness of printed and machined parts and suggested that varying surface height parameters can lead to different frictional behavior. This study presents the techniques for analyzing the surface integrity and periodicity of surface texture resulting from different processing methods. However, this study lacks an investigation of the impact of surface roughness and surface texture on material properties. Existing literature suggest a need of an approach to achieve higher surface quality and reduced internal defects with optimum part performance.

Similarly, the extruder nozzle speed directly governs the material deposition and consequently the surface quality of printing. The majority of literature findings recommend a lower printing speed in the range of 20–25 mm/s to achieve optimal mechanical properties [8,17]. Akande [7] even suggests an optimum printing speed as low as 16 mm/s for superior dimensional accuracy of FFF printed parts. Wang et al. [18] observed unfilled polymers with a printing speed of 20 mm/s yielding the highest tensile strength and density. Increasing print speed revealed negative impacts on the density, tensile strength, and surface quality. The authors attributed this to the inadequate time and energy required for a stronger layer-on-layer bonding of materials during higher printing speeds. This was supported by the presence of fewer voids observed with parts from lower printing speeds. In a follow-up study [19], printing polymer composites at 5 mm/s yielded optimal mechanical properties, printing stability, and superior part quality. Internal defects in the form of massive voids at a maximum velocity of 25 mm/s confirmed the negative effects of increasing printing speed, resulting in the deterioration of mechanical properties. On the contrary, it is important to recognize that printing speed directly determines the overall part fabrication time, where lower printing speed results in prolonged printing time. Recently, Wang et al. [20] proposed a multispeed printing approach capable of controlling printing speed along the part thickness and heat-induced shrinkage strain to reduce the built time and process complexity. Time-extensive part fabrication is usually undesirable as it leads to the unsustainable approach of an energy-extensive manufacturing process. Therefore, reducing the printing time without compromising the material properties is the key to the feasibility of 3D printing.

It is well known that achieving desired material properties of printed parts can be quite challenging due to variable process parameters. Studies show that printing with lower values of layer thickness produces parts with reduced internal voids and layer delamination resulting in superior mechanical properties [21]. Layer thickness as low as 0.2 mm is found to yield the highest tensile strength and stiffness of FFF-printed polymers [22,23]. In a study, ABS parts printed with a unidirectional 0° raster angle are found to exhibit superior tensile strength compared to 90° raster orientation [14]. This is due to the tensile force direction parallel along the length of 0° raster angle allowing for higher resistance to tension, while 90° raster has the lowest resistance. However, the optimal combination of raster angles for enhanced material performance has not yet been fully established and several recommendations can be found in the literature [12,13,24]. With alternating 0°/90° raster orientation, the specimen follows a rule-of-mixture type tensile behavior with equal distribution of 0° and 90° raster over the individual odd and even layers. This results in an approximate average value of tensile strength between the two raster angles, as demonstrated in Refs. [25,26]. On a similar note, +45°/-45° combinations (alternating +45° and −45° raster angles in adjacent layers) also exhibit nearly identical behavior. However, considering the variation in results from the literature, no firm conclusions can be deduced regarding which specific raster angle between 0°/90° and +45°/-45° yields the optimum combination of strength and print quality with reduced defects [14].

The tribological performance of printed parts is influenced by process parameters and plays a crucial role in the effective printing of polymeric load-bearing components [27,28]. Norani et al. [29] showed that the infill structure of FFF-printed ABS significantly impacts the tribological behavior during dry sliding. The correlation between running-in distance and steady-state friction revealed that altering the surface structure changes the contact stress distribution and tribological performance. The worn surfaces revealed abrasive wear debris after a sliding distance of 600 m, where minimum surface roughness resulted in lower wear rates. This study provides critical information on the dry sliding behavior of printed ABS, however, lacks the investigation on the correlation of internal and surface structures with improved friction and wear. Prusinowski and Kaczynski [30] used a pin-on-disc configuration to investigate the tribology of printed ABS-based components. The authors showed a significant difference in the wear behavior of printed parts despite exhibiting comparable coefficients of friction (COF) and linear wear, while applied contact pressure had a greater impact on the friction and wear properties. Bankupalli et al. [31] recently showed that tribological performance under pin-on-disc dry sliding of FFF-printed ABS depends on the build orientation, applied load, and sliding distance. Increasing applied loads reduced the COF but increased the volumetric wear rates, while an increase in sliding speeds increased both COF and wear rates. It is important to note that most of the discussed studies on tribological and mechanical properties of printed polymers have utilized open-system desktop 3D printers without a heated build chamber environment. Such literature findings depict an overview of the tribology of printed polymers, however, still lack a substantial investigation on the influence of processing parameters on friction and wear performance.

This work utilizes an enclosed FFF 3D printer capable of controlling the chamber temperature to fabricate ABS components. Printing under a controlled environment reduces the differences in thermal gradient between the two adjacent layers during fusion and solidification. It is expected that this will lead to reduced internal defects and improved interlayer adhesion, allowing for increased printing speed without compromising the material properties. Thereby, the main aim of this study is to understand the formation and distribution of internal voids as well as surface defects arising from the processing conditions and their impact on part performance. The influence of printing speed and raster angle orientation on the printability, part quality, printing time as well as mechanical and tribological characteristics are investigated. The findings of this study can bridge the existing gap in the interrelationship between the processing-induced defects and corresponding friction and wear performance in material-extrusion 3D printing of polymers.

2. Experimental details

2.1. *Materials and sample preparation*

Experiments were carried out using FFF-printed ABS parts. The 3D CAD models were designed using Solidworks 2018 and exported as STL files into the Simplify3D software for process parameters setting and slicing into layers. Simplify3D generated G-code files were uploaded into the D300-HC 3D printer (D-Force, China) for final printing. ABS feedstock filaments with a diameter of 1.75 mm and a density of 1050 kg/m^3 were obtained from Excelled Northbridge3D, China. Injection-molded ABS procured from Ensinger plastics – TECARAN ABS [32] was used as a reference for the comparison of tribological performances of printed components.

The experimental specimens were printed in horizontal build orientation with two different raster angles (0°/90° and +45°/-45°) and at two different printing speeds (20 mm/s and 50 mm/s). The schematics of the raster angle orientations representing the slicing model are shown in Fig. 1. Tensile testing specimens according to ASTM D638 [33] and three-point bending test specimens according to ASTM D790 [34] were 3D printed for mechanical characterization. For the tribological analysis, $4 \times 4 \times 4$ mm^3 pins were cut from a 3D-printed rectangular block. Fig. 2 presents the schematics of FFF-printed ABS specimens. The choice of feedstock material, printing parameters, and testing conditions were systematically selected from pilot experiments and literature. Table 1 presents a full description of the optimized as well as variable process parameters used. The printed specimens will be referred to by their labels (A, B, C, or D) hereinafter.

2.2. *Measurement of density and void content*

The density of 3D-printed ABS was measured using the immersion method according to ASTM D792 [35]. The theoretical density of ABS was taken as 1050 kg/m^3 and the density of ethanol used for immersion was taken as 785.5 kg/m^3 at 24.5°C for 4 repeated measurements. The void content (also referred to as porosity content) was calculated according to ASTM D2734 [36] based on Eq. (1).

$$V = 100\,(T_d - M_d)\,/\,T_d \tag{1}$$

In this equation, V is void content (volumetric percentage), T_d is theoretical density (kg/m^3), and M_d is measured actual density (kg/m^3).

2.3. *X-ray micro-computed tomography (XMT)*

Zeiss Xradia 510 Versa X-ray micro-computed tomography (XMT) (Carl Zeiss, Pleasanton, USA) was used to investigate the porosity distribution in FFF printed parts. The interior tomography scans were conducted with a 4X magnification,

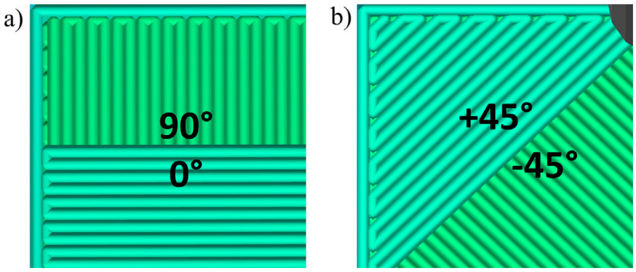

Fig. 1 – Slicing schematics of raster angle orientation: (a) 0°/90° and (b) +45°/-45°.

40 kV source voltage, 3 W source power, 4.04 mm field of view, 4 μm voxel size, and 4 × 4 × 4 mm^3 scanned volume. 2801 projections were acquired with an exposure time of 3 s, and the total scan time was 3.5 h. It should be noted that tomography is a powerful non-destructive technique used for 3D imaging and characterization of the internal structure of materials, however, is still limited by the resolution, field of view, and specimen size depending on the equipment.

The visualizations and porosity analysis from XMT scanned data were obtained using digital image processing software Dragonfly Pro, Object Research Systems (ORS) (Montreal, Canada). The pore segmentation was performed in a multiple-step workflow. Image filtering was carried out using a 3 × 3 × 3 median filter to reduce noise from the dataset. New regions of interest (ROIs) were created using the upper Otsu and lower Otsu thresholding tools to define the intensity domain for reference-ROI and pores-ROI, respectively. The morphological close operation was used to fill the inner spaces on the reference ROI. As a standard procedure, a minimal voxel count of 9 was selected from the pores-ROI for further analysis. Finally, a new multi-ROI was created with all identified pores as separate entities for the calculations of volume fractions and porosity distribution.

2.4. *Mechanical behavior – tensile and flexural properties*

Electroplus 3366 (Instron, USA) universal testing machine is used to perform mechanical characterization of the printed ABS. Tensile testing was conducted with a 10 kN load cell with a speed of 5 mm/min based on the ASTM D638 standard. An axial extensometer of 50 mm gage length was used to measure the strain. Experimentally failed samples were later utilized to investigate the microstructure of tensile fractured surfaces. The flexural behavior was analyzed using a three-point bending test on the same rig equipped with a 10 kN load cell and the crosshead velocity was 1.36 mm/min based on the ASTM D790 standard. All tests were performed five times and an average was calculated for reporting reliable and repeatable data.

2.5. *Microstructure analysis*

Microstructure analysis of fractured surfaces was conducted to understand the fracture behavior and pre-existing internal defects. A JSM-IT300 and a NeoScope JCM – 6000 (JEOL, Peabody, USA) scanning electron microscopes (SEM) were utilized. SEM was also used to investigate the unworn/worn

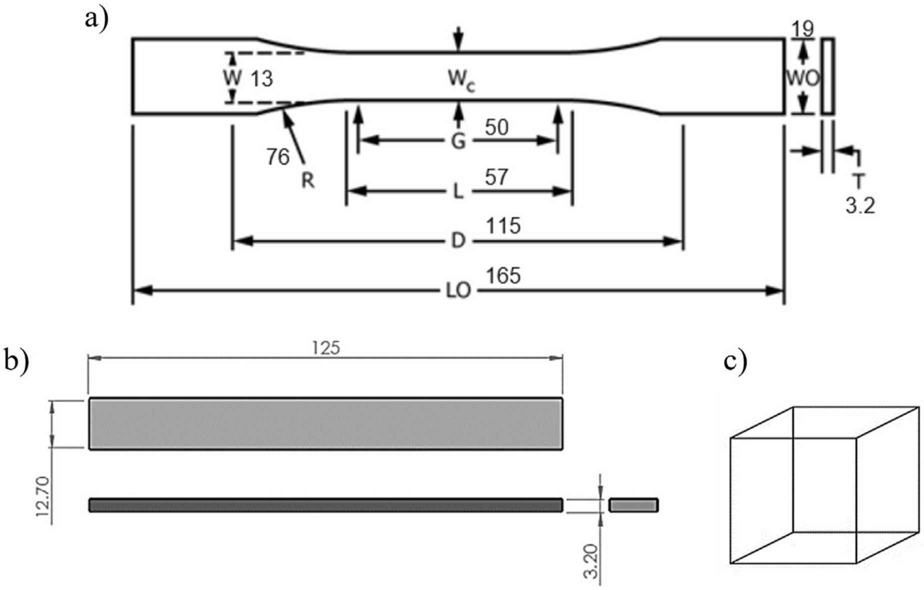

Fig. 2 – Schematics of (a) tensile test specimen (ASTM D638 Type I), (b) flexural test specimen (ASTM D790), and (c) tribological testing pin specimen (4 × 4 × 4 mm^3).

Table 1 – Fused Filament Fabrication (FFF) printing conditions.

Specimen Label	A	B	C	D
Raster angle [deg]	0°/90°	0°/90°	+45°/-45°	+45°/-45°
Printing speed [mm/s]	20	50	20	50
Printing nozzle temperature [°C]	260			
Build platform temperature [°C]	140			
Build chamber temperature [°C]	80			
Extruder nozzle diameter [mm]	0.30 mm			
Layer thickness [mm]	0.20 mm			
Infill pattern	Rectilinear			
Infill density [%]	100%			

surfaces of polymer pins and countersurface plates. All specimens were sputtered with a layer of 15 nm platinum coating before SEM analysis. SEM is an excellent high-resolution technique providing two-dimensional (2D) information required for material characterization and failure analysis. There still is a possibility of artifacts impacting the information obtained, therefore, one should ensure careful coating preparation and data interpretation.

2.6. *As-printed surface topography*

A light optical microscope (LOM), Nikon Eclipse MA200, was used to obtain an overview of the as-printed top surfaces of polymer parts. A scanning white-light interferometer (WLI), Zygo NewView 7300 3D optical profilometer was used to analyze the surface topography. For surface roughness measurements, a 2.5X magnification was used with a 1X field of view resulting in a scan area of 3.15 × 3.15 mm^2. The reported values of surface roughness are the averages of measurements at five different positions on the as-printed top surfaces. MountainsMap Premium 9 analysis software (Digital Surf) was used to perform 2D and 3D analysis of surface roughness profiles of the printed specimens.

2.7. *Tribological characterization*

The friction and wear tests were performed using Cameron Plint TE77 High-Frequency Reciprocating Tribometer (Plint & Partners, Berkshire, England) in a pin-on-plate configuration under dry sliding conditions. 3D-printed ABS pins were used as the reciprocating upper specimen and a stainless-steel plate as a fixed countersurface. Tribological testing specimens were cleaned with ethanol and air-dried before testing. Fig. 3 shows the schematic diagram of the tribological testing configuration. The average sliding speed was kept constant at 0.02 m/s throughout the test duration of 6 h. The applied normal loads of 80 and 160 N were used to generate the initial apparent contact pressures of 5 and 10 MPa, respectively. For simplicity, testing conditions for contact pressures and sliding velocity are used to imitate high-load and low-speed sliding conditions. Table 2 presents the full description of the parameters used for the tribological testing. All the reported friction and wear data are the averages of three repeated tests.

Friction coefficients are recorded directly by data-acquiring software linked with the TE77 tribometer. The vertical displacement experienced by the pin face in contact with the counter surface is continuously measured by the linear variable differential transformer (LVDT) sensor attached to the tribometer. The linear wear of the polymer pin is used to calculate the total volume loss due to pin wear. The specific wear rate coefficient (*Sw*) of the printed specimen is determined based on Eq. (2):

$$S_W = \frac{Total\ volume\ loss\ (\Delta V)}{Normal\ applied\ load\ (F_N)\ x\ Total\ sliding\ distance\ (S_d)} \frac{(mm^3)}{(N.m)} \quad (2)$$

2.8. *Statistical analysis*

The significance of differences between the tribological results obtained for printed ABS was identified via statistical analyses of variance (two-way ANOVA) with a significance level (alpha value) of 0.05 using the software OriginPro 2020 (OriginLab, USA). The dataset and analysis report from ANOVA are included in the Supporting information.

3. Results and discussion

3.1. *Measurement of density and void content*

Table 3 presents the average values of measured densities and void contents (volumetric percentage) of 3D-printed ABS parts. The actual densities of printed samples are similar to the theoretical density of 1050 kg/m^3 of ABS. The calculated maximum void content is 3.54% for specimen D printed with +45°/-45° raster angle orientation at 50 mm/s printing speed. It can be noted that increasing the printing speed for +45°/-45° specimens resulted in reduced density and increased void content, whilst minor variation was recorded for 0°/90° specimens. Further investigations on the void formation and porosity distribution are performed with tomography scans and fractured surface analysis of the printed specimens.

3.2. *X-ray micro-computed tomography (XMT)*

FFF-printed ABS specimens were analyzed using XMT for the characterization of internal defects arising from the processing. The influence of raster angle orientation and printing speed on the distribution and morphology of pores were

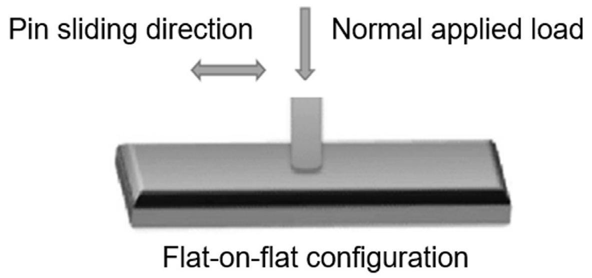

Fig. 3 – Schematic representation of the flat-on-flat tribological testing configuration.

Table 2 – Experimental conditions for tribological tests.

Parameters	Values
Apparent contact pressure	5, 10 MPa
Applied normal load	80, 160 N
Indicated rotor frequency	2 Hz
Stroke length	5 mm
Sliding speed	0.02 m/s
Test duration	6 h
Total sliding distance	432 m
Polymer specimen	4 × 4 × 4 mm^3
Stainless steel plate, grade 316	S_a 0.25 ± 0.02 μm
Temperature	RT (23–25 °C)

Table 3 – Actual density and calculated void content of the printed specimens.

Specimen	Raster angle [deg]	Printing speed [mm/s]	Average actual density measured, M_d [kg/m^3]	Void content, V
A	0°/90°	20	1021.5 ± 1.0	2.71%
B	0°/90°	50	1021.2 ± 1.4	2.74%
C	+45°/-45°	20	1022.0 ± 1.1	2.67%
D	+45°/-45°	50	1012.8 ± 1.3	3.54%

explored with porosity segmentation. Fig. 4 presents the 3D visualizations of the internal microstructure with the distribution of existing pores from tomography scans.

The volumetric porosity (internal void content) within the scanned regions of specimens A, B, C, and D are 4.16%, 6.43%, 2.06%, and 4.20%, respectively. Quantification of segmented pores with minimal 9 voxel counts show a total of 2719, 5163, 2271, and 2467 pores for specimens A, B, C, and D, respectively. The increase in printing speed resulted in relatively higher volumetric porosity as well as higher pore counts. Micropores with a volume size lower than 0.0001 mm^3 contribute to the majority of void content and are distributed throughout the specimen, mostly as voids between the infill of single beads within the same layer. +45°/-45° specimens showed lower content of micropores on the material infill compared to 0°/90° specimens, observed as small dots in Fig. 4. All printed specimens exhibit a similar pattern of formation and distribution for pores above 0.0001 mm^3 volume size, accounting for 150, 170, 166, and 168 pores for specimens A, B, C, and D, respectively. However, increased printing speed exhibits higher content of pores between the individual layers. The pores above 0.001 mm^3 volume size are formed as a connected network of voids between the layers and adjacent raster beads exhibiting 22, 91, 26, and 75 large pores for specimens A, B, C, and D, respectively. The detailed analysis of pore-volume distribution revealed that pores smaller than 0.001 mm^3 contribute to less than 3% of the total pores existing inside the tested specimens. The layer-on-layer nature of the fabrication process induces such networks of void along the raster orientation and is found to be more prominent at higher printing speeds. Therefore, it can be said that increased printing speed influences void formation and interlayer bonding. The volume histograms for porosity distribution and 2D tomography micrographs of each specimen as well as a video animation representing porosity distribution can be found in the Supporting information (Figs. S1–S6 and Video SV1).

Supplementary video related to this article can be found at doi:10.1016/j.jmrt.2023.01.086

3.3. *Mechanical behavior – tensile and flexural properties*

The tensile stress-strain curves of 3D printed ABS with varying printing speeds and raster angles are shown in Fig. 5. The deformation of individual specimens before fracture can be evaluated from the stress-strain curves. The curves corresponding to 0°/90° specimens exhibited relatively lower elongation at break without obvious necking compared to +45°/-45° specimens. A and B strained slightly and suffered a fracture after yielding, while C and D sustained higher strain with a gradual drop in stress after yielding. C and D exhibited more than 60% increase in elongation at break, indicative of higher material toughness [37] for printed parts with +45°/-45° raster angles.

Table 4 shows the tensile and flexural properties of the printed specimens. Higher tensile strength and young's modulus were observed with +45°/-45° raster angle orientation. In any printing layup with combined raster angle orientation, the final mechanical strength is usually the average result of two raster combinations, as suggested in Refs. [25,26]. Therefore, a stronger interfacial bonding between adjacent raster beads will lead to improved tensile strength. In a 0°/90° orientation, the individual raster beads parallel to the loading direction contribute to the majority of tensile load bearing, whilst the perpendicular raster beads are prone to cleavage. This differs with the strength of +45°/-45° specimens, highly depending on raster bonding as the direction of printing with crisscross orientation will not have the same influence as the parallel/perpendicular orientation.

For both raster angle orientations, the influence of increased printing speed was insignificant considering the tensile properties, indicating that printing under a temperature-controlled environment increases the interlayer bonding. The enclosed chamber helps to reduce the temperature gradient between individual raster beads leading to the optimized cooling of the deposited material even at an increased printing speed. This results in improved adhesion and fusion of the individual layers enhancing the material strength. Fig. 6 shows the comparison of tensile strength and measured void content for printed specimens. It can be observed that despite the higher porosity content for +45°/-45° specimens at higher printing speed, there was an insignificant impact on the tensile strength of tested materials.

Higher flexural properties can be observed with +45°/-45° raster angle orientation compared to 0°/90°. For 0°/90° specimens, increasing the printing speed reduced the flexural strength by 8% and flexural modulus by 6%. +45°/-45° specimens with crisscross orientation showed increased bending resistance compared to 0°/90° raster angles. It can also be observed that increasing the printing speed shows an insignificant deviation in the flexural properties of +45°/-45° specimens. Note that printed ABS in this study exhibited improved tensile and flexural properties compared to the recent findings from the literature [13,38].

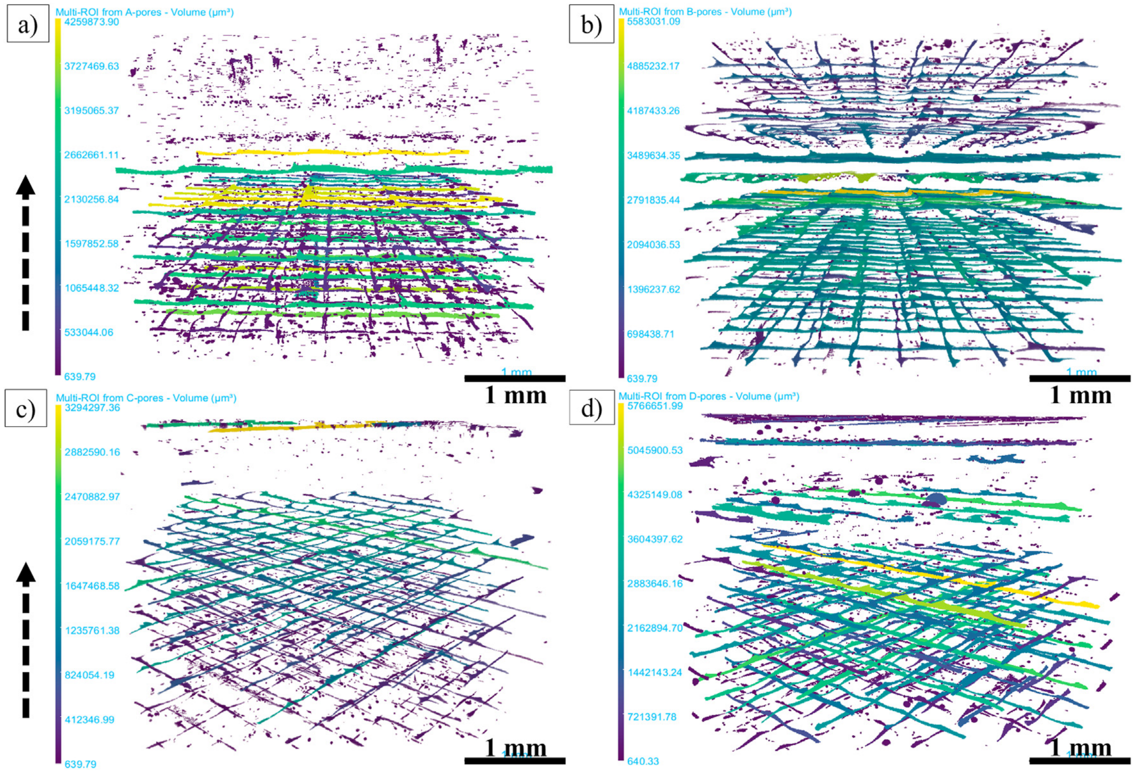

Fig. 4 – XMT 3D visualization of all pores observed in printed ABS: (a) 0°/90° raster angle, 20 mm/s printing speed; (b) 0°/90° raster angle, 50 mm/s printing speed; (c) +45°/-45° raster angle, 20 mm/s printing speed; (d) +45°/-45° raster angle, 50 mm/s printing speed (arrow indicates material deposition in Z direction).

3.4. *Microstructure analysis*

The tensile test-fractured surfaces of all printed specimens were studied with SEM. For all printed specimens, three types of internal defects in the form of voids were observed. Fig. 7 shows the schematic representation of deposited material with the locations of different types of voids. First, micropores were formed between the material infill on the single bead of deposited filament (indicated with red arrows). Second, voids were formed between the individual layers in the direction of deposition indicating the layer separation (indicated with yellow ovals). Lastly, voids were formed in-between the fusion of adjacent raster beads and in-between the beads deposited within the nth layer and (n+1)th layer (indicated with violet triangles), Fig. 7.

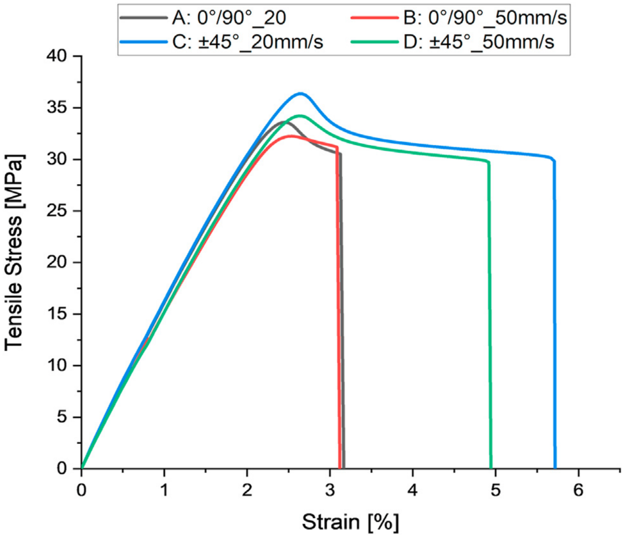

Fig. 5 – Stress-strain curves for 3D printed ABS under tension: A: 0°/90° raster angle, 20 mm/s printing speed; B: 0°/90° raster angle, 50 mm/s printing speed; C: +45°/-45° raster angle, 20 mm/s printing speed; D: +45°/-45° raster angle, 50 mm/s printing speed.

3.4.1. *Fractured surface analysis of 0°/90° raster angle specimens*

The microstructure of fractured surfaces of 0°/90° specimens (A and B) exhibited mostly smooth fracture with the presence of striations and abrupt steps, as seen in Figs. 8 and 9. Such abrupt steps occurred due to the cleavage of adjacent raster and individual layers, an indication of brittle fracture mode. SEM overview of 0°/90° specimens in Figs. 8(a) and 9(a) clearly shows voids along the layer boundary. Similarly, crater-like voids on the fractured surfaces resulting from the air pockets can be observed in Fig. 8(b).

The fractured section of 0°/90° specimens also showed chevron patterns and nearly flat surfaces originating from the voids without the regions of deformation, presented in Figs. 8(d) and 9(d). The initiation of these regions was found in the voids between the adjacent raster beads. Fine and small

Table 4 – Mechanical properties of 3D printed ABS.

Specimen	Tensile strength [MPa]	Young's modulus [GPa]	Flexural strength [MPa]	Flexural modulus [GPa]
A	34.35 ± 0.70	2.33 ± 0.03	55.57 ± 1.10	2.06 ± 0.03
B	34.45 ± 1.44	2.31 ± 0.09	50.74 ± 1.16	1.92 ± 0.05
C	36.21 ± 1.28	2.44 ± 0.03	58.71 ± 1.16	2.00 ± 0.07
D	36.16 ± 1.13	2.36 ± 0.04	58.08 ± 0.47	1.99 ± 0.01

cracks often initiate from the weakest point of printed parts either due to pre-existing pores or internal defects. Such small cracks connect to form a network and propagate with ridge and valley markings until the specimen fails under tension. The flat rupture observed with the river line marks indicates that brittle fracture is the dominant mode of failure. Wu et al. [39] earlier observed similar tensile failure behavior initiating at the weakest raster point and propagation to the adjacent raster until the failure of 3D printed ABS.

It is interesting to see voiding on the edges of fractured surfaces for some 0°/90° specimens, represented in Fig. 8(c). Voiding on the edges occurs due to heat-dissipating off the perimeter which restricts polymer diffusion. However, such a defect is not representative of the entire printed component and only occurs on the outline of FFF printed objects. The voiding on edges can be reduced by depositing material on the perimeter at a lower speed than the actual infill printing. The reduction in outline speed allows for a better solidification process on the perimeters and helps to achieve higher surface quality reducing such internal defects.

3.4.2. *Fractured surface analysis of +45°/-45° raster angle specimens*

The morphology of fractured surfaces of +45°/-45° specimens (C and D) are presented in Figs. 10 and 11. The presence of deformed fibrils suggests that +45°/-45° raster angle orientation leads to moderately ductile fracture behavior under tension. Morphological analysis of the test-failed surface of specimen C with lower printing speed showed that interlayer defects induce the manifestation of stress fields closer to circular structures and act as the regions of stress concentration. The circular/spherical stress fields, as seen in Fig. 10(d), are indicative of a mixed fracture mode. The microcrack formation, crack growth and crack propagation occur from such pre-existing defects, observed as the whitish V-shaped pattern in Fig. 10(a). Microstructure analysis of almost all fractured surfaces shows that failure occurred in these whitened regions originating from voids between raster beads, evident from the scanning electron micrographs. The appearance of such whitish fibrils on the surfaces can be associated with crazing or hairline craze cracking which occurs due to localized failure resulting from residual stresses [37]. This phenomenon can be reduced by controlling the formation of voids. Typically, voids form as a consequence of the noncompact arrangement of individual raster beads and gaps originating due to the improper bonding of material infill.

In contrast to 0°/90° specimen, only a few crater-like voids between the infill and among the layers were observed for +45°/-45° raster angles with lower printing speed, as seen in Fig. 10. However, higher printing speed (specimen D) resulted in large voids between the adjacent raster beads and layers, Fig. 11(c). The analysis of failure regions of specimen D also exhibited mirror, mist, and hackle morphology, represented in Fig. 11(b), usually associated with a brittle fracture [40]. The reduction of elongation at break with increased printing speed for +45°/-45° specimens in section 3.3 supports the observed fracture behavior. This suggests that printing speed can influence the mode of fracture. Micrographs for specimens fabricated at higher printing speeds (B and D) also exhibited larger voids between the layers and individual raster beads, Figs. 9 and 11. The observation from porosity analysis of XMT scans in section 3.2 supports the presence of higher void content in the form of a larger connected network of voids for specimens with increased printing speed. Thereby, increased printing speed can influence the interlayer adhesion, while such existing voids consequently act as stress concentrators [41].

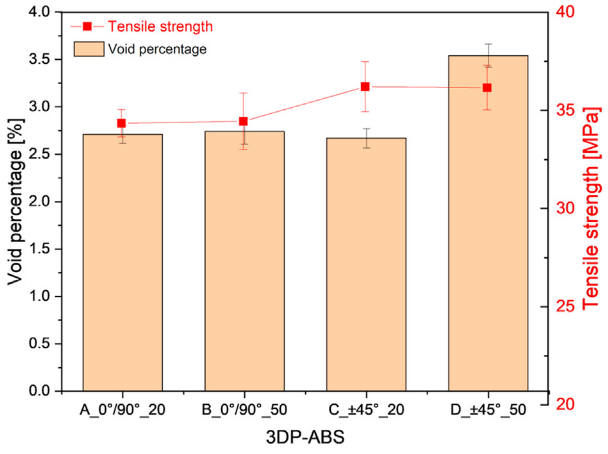

Fig. 6 – Comparison of tensile strength and void content of printed specimens: A: 0°/90° raster angle, 20 mm/s printing speed; B: 0°/90° raster angle, 50 mm/s printing speed; C: +45°/-45° raster angle, 20 mm/s printing speed; D: +45°/-45° raster angle, 50 mm/s printing speed.

3.5. *As-printed surface topography*

Light optical microscopic analysis of FFF parts showed deposition paths and uneven stacking of materials on the top surface along the print head running direction (indicated with white arrows), Fig. 12. Filament traces and excess material looking like hills were observed on the top face. This is due to the squeezing action of the nozzle leading to the material overlapping with newly deposited beads forming hills and grooves along the print path. This can result in coarser topography of the top surfaces as no further material deposition occurs to compensate for the unevenness of

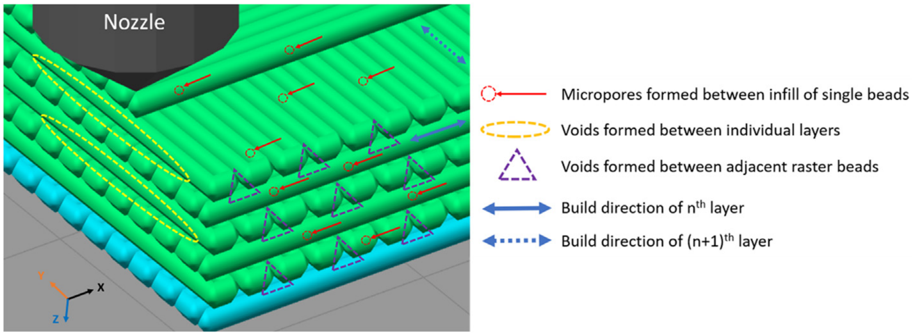

Fig. 7 – Schematic representation of the location of different voids.

consecutive peak heights and valley depths. Increased printing speed showed visible differences in filament traces with the uneven spreading of deposited materials for both raster angle orientations, Fig. 12(b, d).

The measured surface roughness values of printed parts using a 3D profilometer are presented in Table 5. Both varying raster angles and printing speed influenced the as-printed surface roughness. +45°/-45° specimens (C and D) showed relatively higher surface roughness compared to 0°/90° specimens. The measured surface roughness (Sa) values were in the range of 8–20 μm. Increased printing speed resulted in slightly increased surface roughness values for all specimens. During higher printing speeds, surface roughness can be a critical issue as enough time is not allowed for the deposited material to regain its resistance against nozzle shearing during the next print path. Usually, open-system FFF-printed parts are known to have a rough surface texture resulting from the staircase effect [42]. Even a small-scale warping or curling of single layers can vary the texture formation and consequently the surface roughness

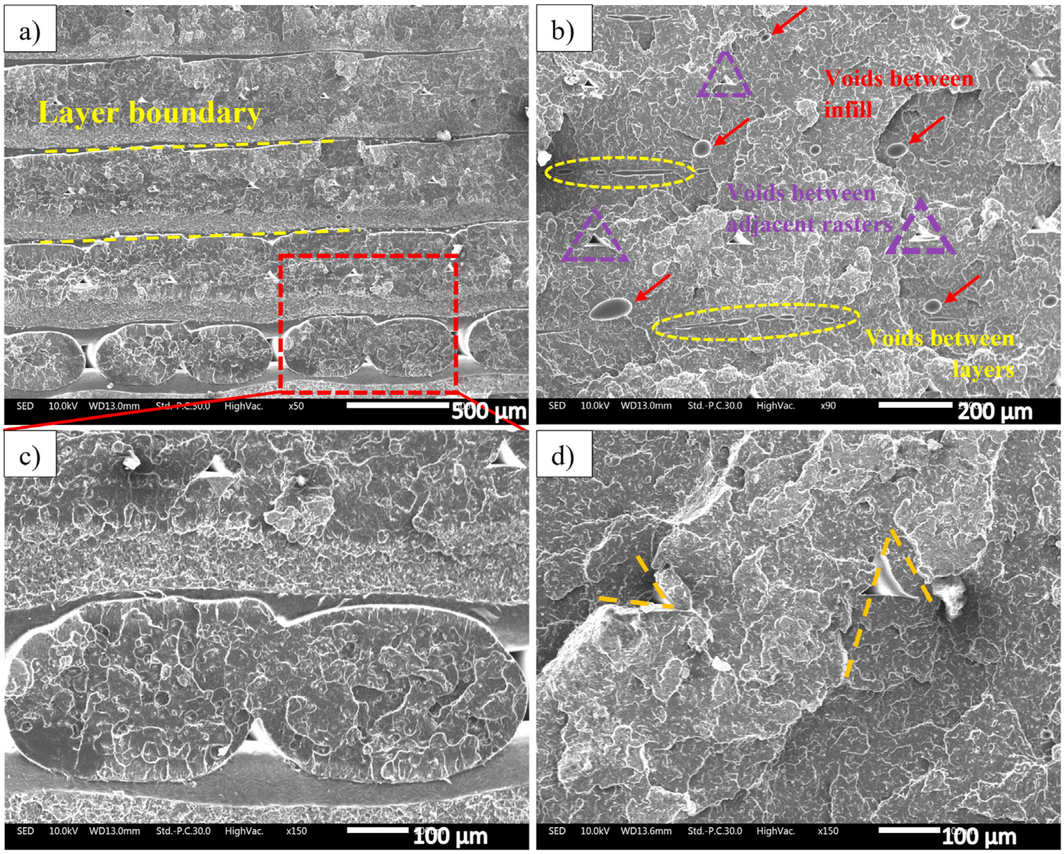

Fig. 8 – SEM micrographs of fractured surfaces of specimen A: 0°/90° raster angle orientation, 20 mm/s printing speed; (a) overview indicating layer boundaries, (b) crater-like voids, (c) magnified view indicating voiding at edges, (c–d) failure regions.

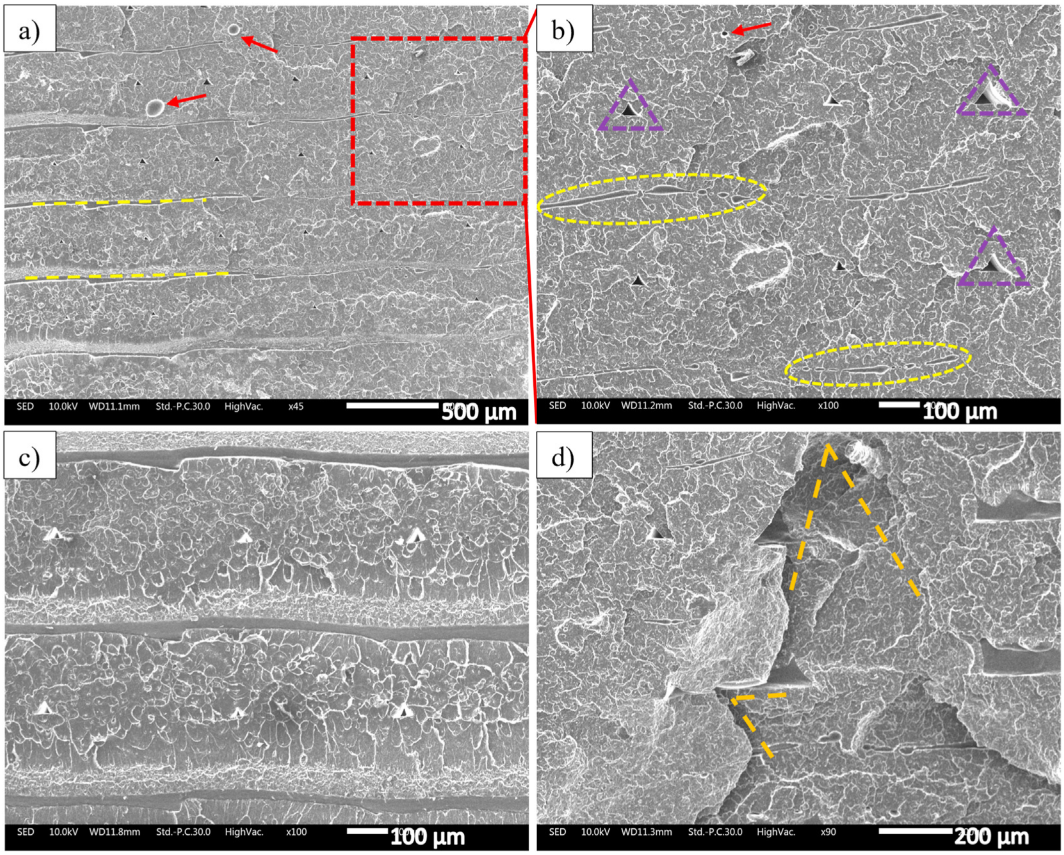

Fig. 9 – SEM micrographs of fractured surfaces of specimen B: 0°/90° raster angle orientation, 50 mm/s printing speed; (a, b, c) overview indicating layer boundaries and voids, (d) failure regions.

of fabricated parts. Minor altercations on the individual layers can lead to the deformation of individual surface textures during solidification, which can change the surface height parameters of as-printed surfaces. This can be minimized with a slow and steady cooling that allows interlayer fusion and solidification within a similar temperature range. The improved surface quality of printed ABS in this study can be attributed to the controlled build environment improving the bonding of newly deposited materials even at a higher printing speed, consequently improving the surface roughness.

The surface quality of printed parts greatly depends on printing speed, printing temperature, nozzle diameter, and layer thickness. However, optimization of FFF process parameters has not been able to eliminate the rough textures completely. Post-processing techniques such as heat treatment, laser treatment, chemical vapor polishing, and grinding were found to improve the surface quality of printed ABS parts [43]. Chemical surface treatments with acetone were reported to drastically improve the surface roughness of printed ABS. The average surface roughness (Ra) of printed ABS reduced from 185.4 μm to 57.6 μm (immersion in acetone solution for 5 s each in 2 intervals) [44]. Similarly, acetone vapor polishing effectively reduced surface roughness (Ra) from 37.18 μm to 10.13 μm after 45 min exposure [45], while laser polishing treatment for 60 s was reported to improve the surface quality reducing the roughness from 18.5 μm to 0.24 μm [46]. Although, the lack of dimensional accuracy, chemical emissions, increased overall production time, and associated costs are the negative impacts of post-processing.

To further understand the surface topography and texture of printed specimens, 2D and 3D analyses of primary surface profiles were obtained within a scan area of 3.15 × 3.15 mm^2. The profile slicing was performed in X and Y directions along the print orientation (XY plane on top face) to examine the periodicity of peak heights and valley depths on the as-printed top surfaces. 2D surface topography of 0°/90° specimens and +45°/-45° specimens are presented in Figs. 13 and 14, respectively. Fig. 15 presents the 3D view of all the analyzed surfaces (A, B, C, and D).

For 0°/90° specimens (A and B), periodicity of peak heights and valley depths for sliced 2D profiles were consistent along the Y direction (slice i), while inconsistent variations were observed in the X direction (slices ii and iii), as seen in Fig. 13. This inconsistency arises from the inhomogeneous material deposition on the top surfaces and applies to both printing speeds, as observed from the optical micrographs. On the other hand, +45°/-45° specimens (C and D) showed similar periodicity of peak heights and valley depths along both slicing directions, as seen in Fig. 14. The periodicity pattern and distribution of hills and grooves are also revealed from the

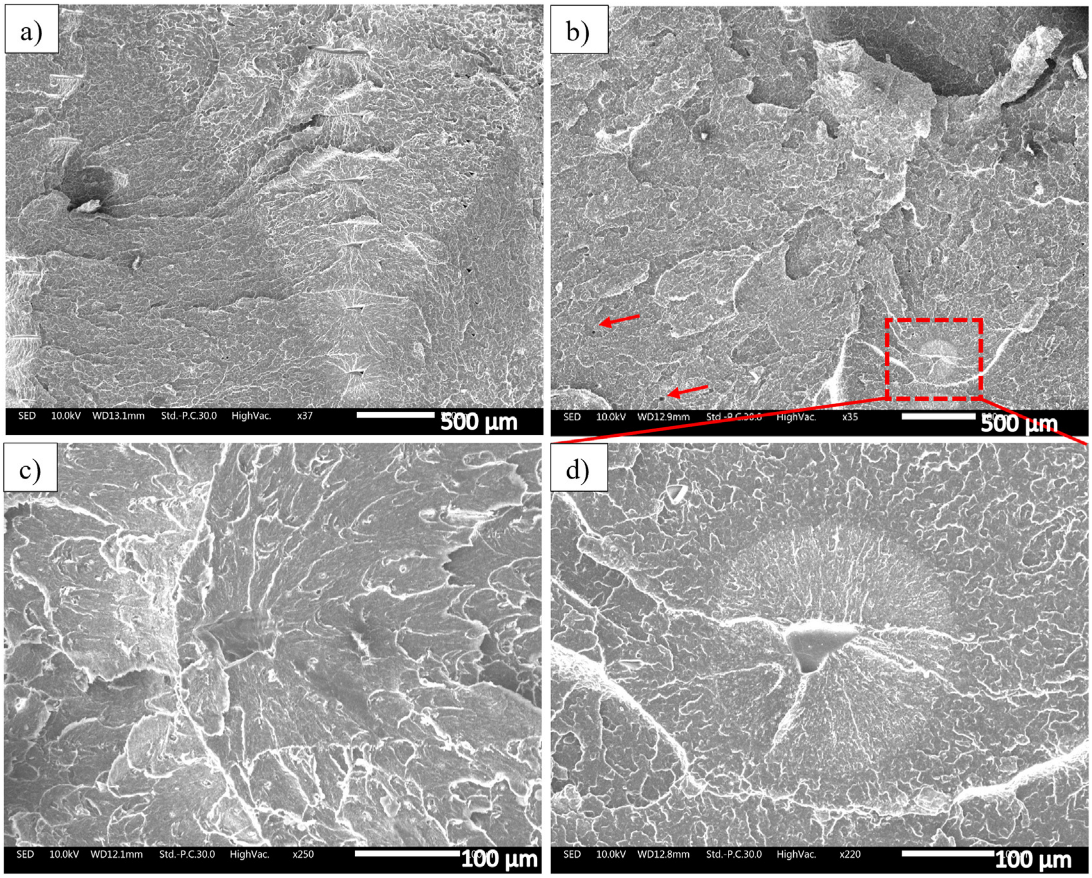

Fig. 10 – SEM micrographs of fractured surfaces of specimen C: +45°/-45° raster angle, 20 mm/s printing speed; (a–b) overview indicating voids and failure patterns, (c–d) magnified view of failure regions.

3D view of the as-printed top surfaces, Fig. 15. Higher printing speed did not influence the periodicity of peaks and valleys for all 0°/90° and +45°/-45° specimens. However, increased peak heights and valley depths were observed from the analysis of primary surfaces and slicing profiles for specimens with higher printing speeds, Figs. 13(b) and 14(b). This can be explained by the stacking of infill materials due to the increased nozzle squeezing at higher printing speeds.

In this study, maximum profile heights (Rz) of 58.7, 69.15, 45.37, and 52.97 μm were measured for tested specimens A, B, C, and D, respectively. Yang et al. [47] recently reported maximum profile heights (Rz) for printed ABS in the range of 76.4–86.4 μm with a layer thickness of 0.2 mm and 100 mm/s printing speed. Similarly, open-system desktop printers were reported to produce ABS surfaces with average surface roughness (Ra) of 65 μm with a printing speed of 30 mm/s and 0.1 mm layer thickness [48], while 0.25 mm layer thickness showed Ra up to 40 μm [45,49]. The average surface roughness (Ra) for specimens A, B, C, and D was found 12.41, 16.10, 11.13, and 13.22 μm, respectively. Similar roughness values (Ra) were reported in Ref. [15], a maximum of 18.8 μm for a layer thickness of 0.25 mm and 30 mm/s print speed.

In addition, skewness (Ssk) and kurtosis (Sku) parameters of the as-printed surfaces were also studied. As suggested in Ref. [50], Ssk and Sku parameters further indicate the surface structure and shape of the profiles of additively manufactured parts. The positive values of the skewness parameter, $Ssk > 0$, for all specimens suggests the distribution of peaks dominant over valleys on the printed surfaces. Kurtosis parameters indicated a higher concentration of sharp peaks and deep valleys on the surfaces of specimens A ($Sku = 4.02$) and B ($Sku = 2.99$) compared to C ($Sku = 2.49$) and D ($Sku = 2.12$), supporting the relatively broader peaks and valleys observed for +45°/-45° specimens, Fig. 14. The detailed analysis of height parameters from the primary surface profiles measured along all slicing planes is presented in the Supporting information (Tables S1 and S2).

2D and 3D surface profiles exhibited differences in roughness periodicity and distribution of peaks and valleys on the top surfaces of printed parts. The processing conditions resulting in such irregularities can provide a significant impact on polymer-steel contact surfaces while sliding under loaded conditions. The variation in material deposition structure can influence the shearing and removal of materials on tribo-contact and result in varying friction and wear behavior of the printed polymers over time.

3.6. *Tribological characterization*

3.6.1. *Time-dependent frictional behavior*

As observed in Fig. 16, the evolution of friction coefficients with time shows an initial spike due to irregular surface

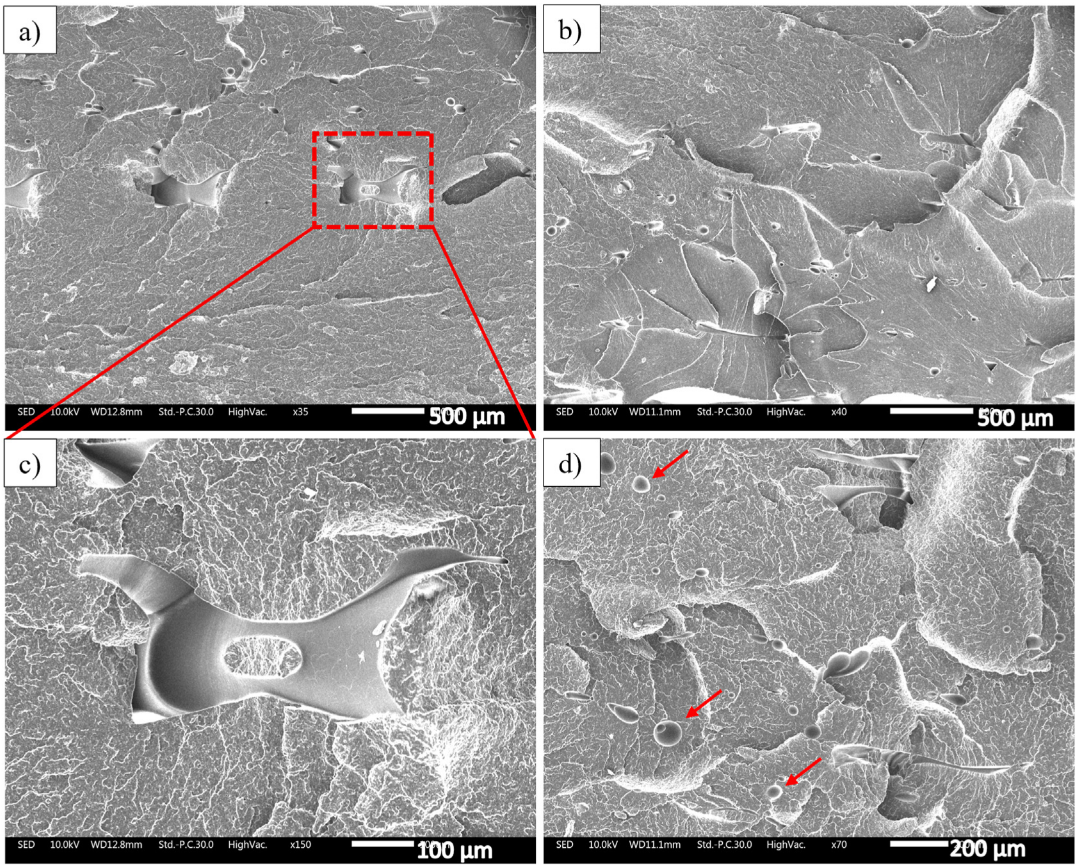

Fig. 11 – SEM micrographs of fractured surfaces of specimen D: +45°/-45° raster angle, 50 mm/s printing speed; (a–b) overview indicating voids and failure patterns, (c–d) magnified view of failure regions.

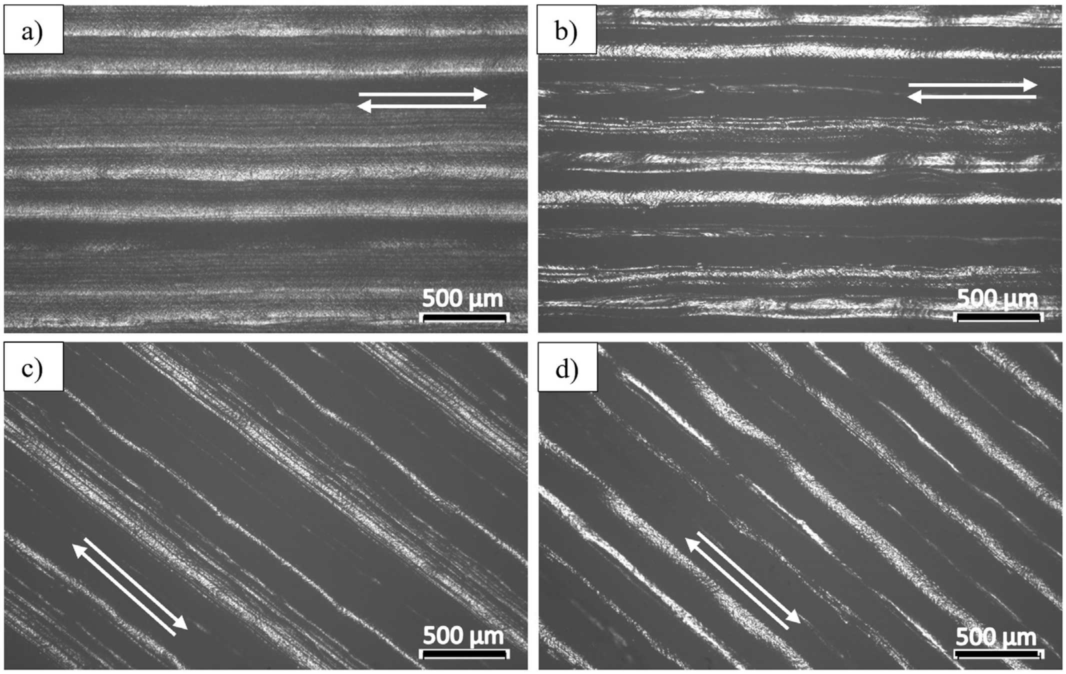

Fig. 12 – Optical micrographs showing as-printed top surfaces (scale 500 µm): (a) 0°/90° raster angle, 20 mm/s printing speed; (b) 0°/90° raster angle, 50 mm/s printing speed; (c) +45°/-45° raster angle, 20 mm/s printing speed; (d) +45°/-45° raster angle, 50 mm/s printing speed.

Table 5 – Surface roughness, Sa values for printed ABS.

Specimen	Surface roughness, S_a [µm]
A	8.67 ± 0.5
B	13.93 ± 0.7
C	17.09 ± 0.5
D	19.08 ± 0.7

contact between the tribo-materials. The excess material as hills and uneven deposition along the print path was observed from optical micrographs of as-printed top surfaces. Such coarser asperity peaks cause an initial increase in friction coefficient during the running-in phase due to plastic deformation. The friction-time curves attained a steady-state regime when rough surface asperities are deformed and polished to attain stable contact after almost 60 min of the test. It should be noted that all specimens sliding under 10 MPa contact pressure (equivalent to 160 N normal load) achieved early steady-state regimes compared to 5 MPa (equivalent to 80 N normal load). This can be attributed to the earlier deformation of rough asperities in the contact zone resulting in smoother surface topography under increased applied load. This phenomenon agrees with studies where similar trends were reported for increased applied loads resulting in early steady-state friction regimes for 3D printed polymers under dry sliding conditions [10,29,31].

For 0°/90° raster angle specimens (A and B), COF over time does not show significant variation with increasing loads during the steady-state regime, Fig. 16(a). The steady-state COF stays at around 0.20 for all tested specimens. However, it should be noted that specimens printed at 50 mm/s speed showed a longer running-in period before achieving a steady-state regime compared to the specimens with 20 mm/s printing speed. The reason for this phenomenon is the higher surface roughness resulting from higher printing speed leading to a delayed running-in phase. Nevertheless, there is no significant influence of printing speed on the frictional response during the steady-state regime.

In contrast, +45°/-45° raster angle specimens (C and D) showed reduced COF over time with increasing applied loads, Fig. 16(b). It was found that +45°/-45° specimens exhibited higher elongation at break, yield stress, and modulus compared to 0°/90° specimens in section 3.3. During sliding at high contact pressure, polymer materials show a directly proportional relationship between the material properties and resistance to deformation [51]. The reduced COF with increasing loads for C and D specimens can be attributed to their higher toughness and ductile behavior. On a similar note, +45°/-45° specimens with higher material properties are

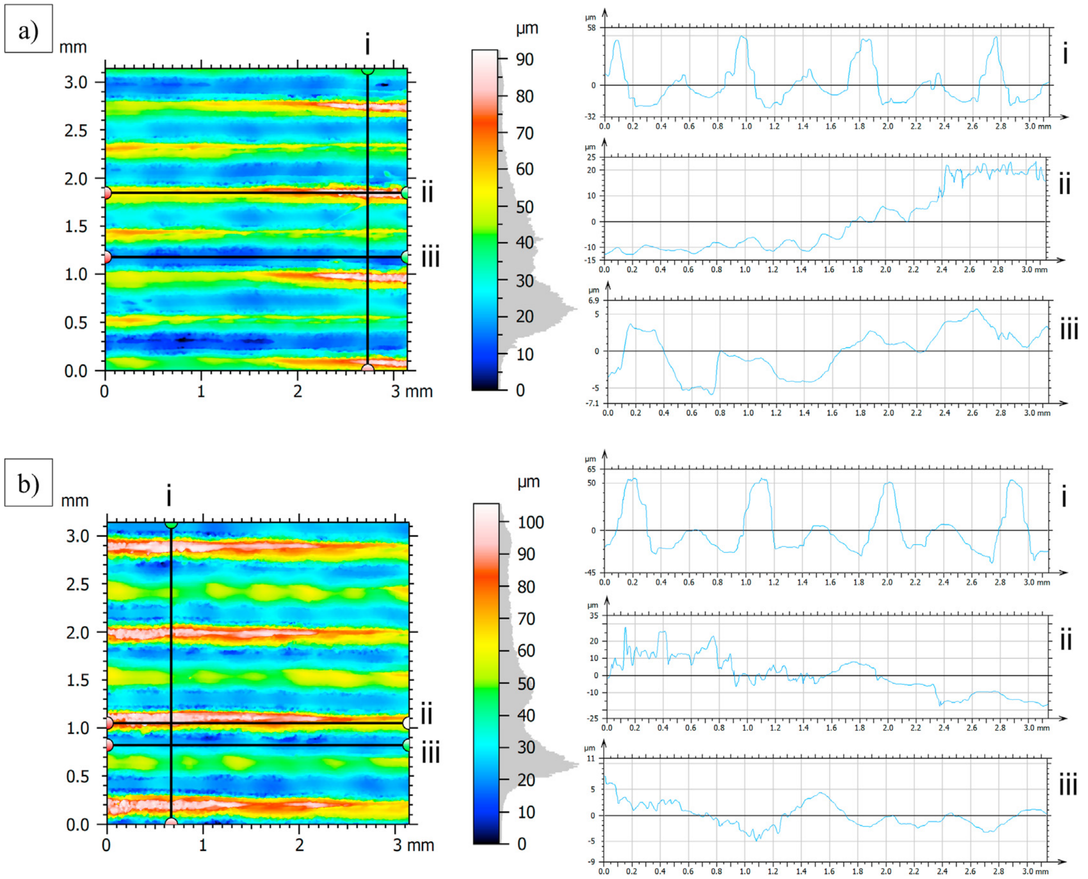

Fig. 13 – Primary surface and 2D slicing profile of printed ABS with 0°/90° raster angle orientation indicating the periodicity of peak heights and valley depths along the Y direction (slice i) and X direction (slice ii and iii): (a) 20 mm/s printing speed (Specimen A); (b) 50 mm/s printing speed (Specimen B).

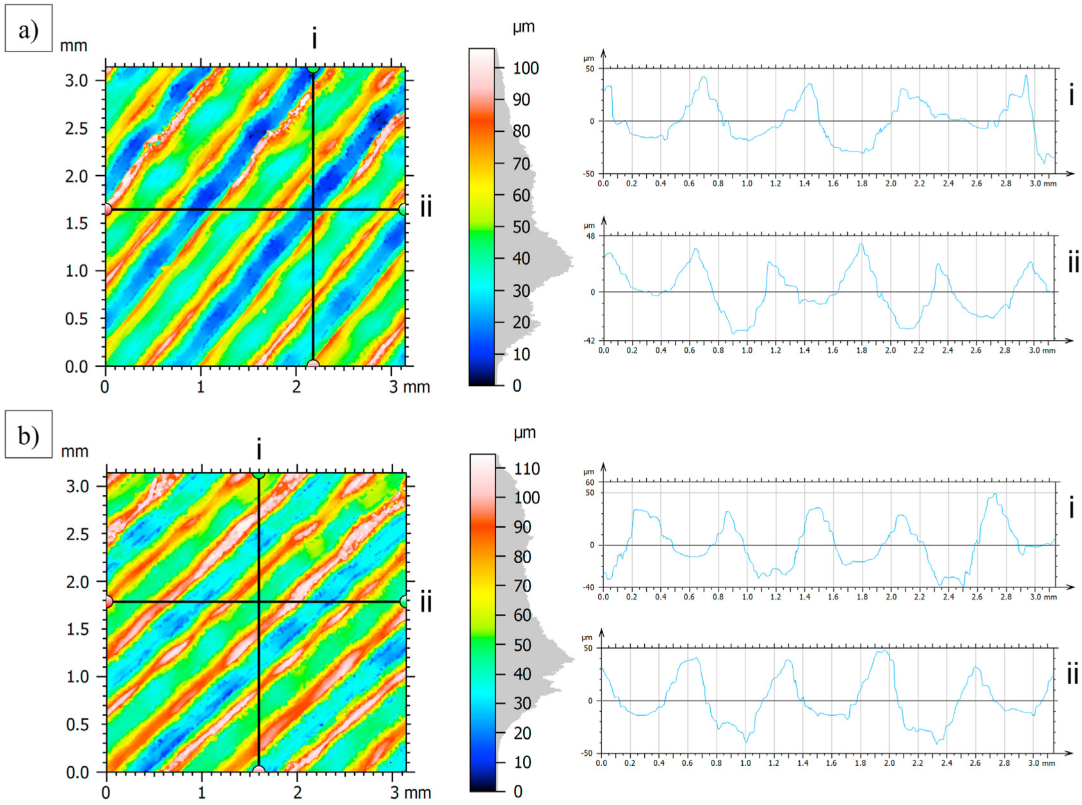

Fig. 14 – Primary surface and 2D slicing profile of printed ABS with +45°/-45° raster angle orientation indicating the periodicity of peak heights and valley depths along the Y direction (slice i) and X direction (slice ii): (a) 20 mm/s printing speed (Specimen C); (b) 50 mm/s printing speed (Specimen D).

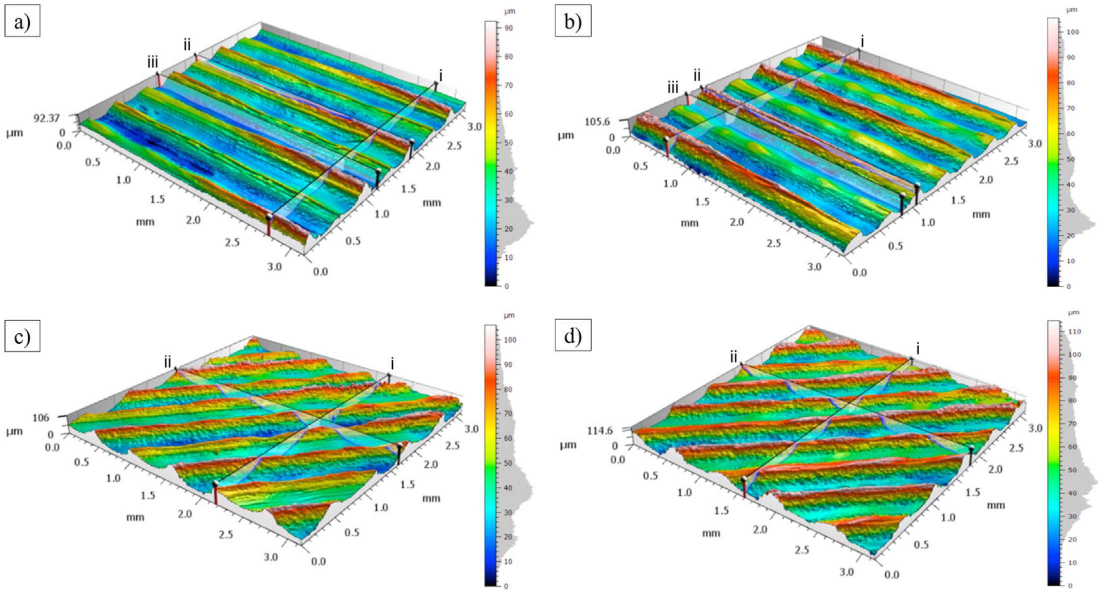

Fig. 15 – 3D morphology of top surfaces of printed specimens: (a) 0°/90° raster angle, 20 mm/s printing speed (Specimen A); (b) 0°/90° raster angle, 50 mm/s printing speed (Specimen B); (c) +45°/-45° raster angle, 20 mm/s printing speed (Specimen C); (d) +45°/-45° raster angle, 50 mm/s printing speed (Specimen D).

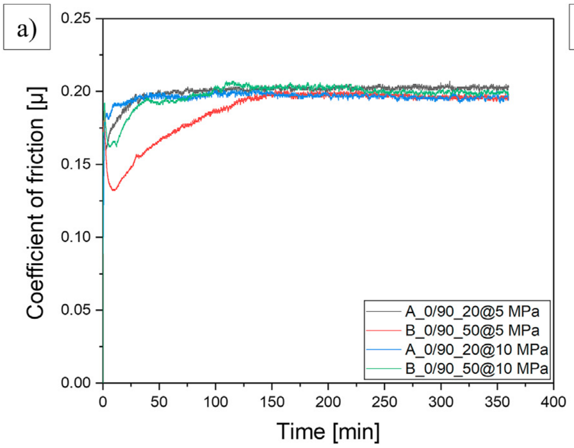

Fig. 16 – **Evolution of friction coefficient with time under varying contact pressure and printing speeds: (a) 0°/90° raster angle and (b) +45°/-45° raster angle.**

expected to exhibit increased resistance to ploughing and surface damage.

3.6.2. *Average steady-state COF*

The average steady-state coefficients of friction are presented in Fig. 17. The dry sliding COF values for printed ABS are in the range of 0.18–0.23 under 5 and 10 MPa contact pressures. Specimens A and B with 0°/90° raster angles showed almost no change in the average COF with increased applied load. The highest COF of 0.23 is observed with +45°/-45° specimen under 5 MPa contact pressure. +45°/-45° specimens (C and D) showed a reduction in COF when applied normal loads were increased. This agrees with the time-dependent frictional behavior of specimens C and D observed in section 3.6.1. Similar COF reductions with increasing applied loads during dry sliding of FFF-printed ABS were found in relevant studies [30,31].

On the other hand, increased printing speed did not influence the average steady-state COF of all printed specimens under both loading conditions, confirmed by two-way ANOVA. Increasing the applied loads for all 0°/90° specimens showed statistically insignificant differences with $p = 0.844 > 0.05$, while all +45°/-45° specimens showed statistically significant differences with $p = 0.009 < 0.05$. The variation in printing speeds for both raster angle orientations showed statistically insignificant differences, $p = 0.216 > 0.05$ for 0°/90° specimens and $p = 0.231 > 0.05$ for +45°/-45° specimens, presented in the Supporting information (Figs. S7 and S8). This suggests that it is possible to print at higher speeds

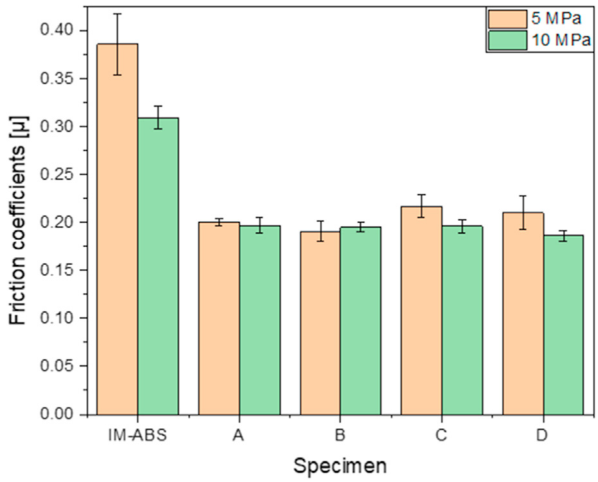

Fig. 17 – **Average steady-state coefficients of friction at 80 N and 160 N for injection molded (IM-ABS) and 3D printed ABS (A: 0°/90° raster angle, 20 mm/s printing speed; B: 0°/90° raster angle, 50 mm/s printing speed; C: +45°/-45° raster angle, 20 mm/s printing speed; D: +45°/-45° raster angle, 50 mm/s printing speed).**

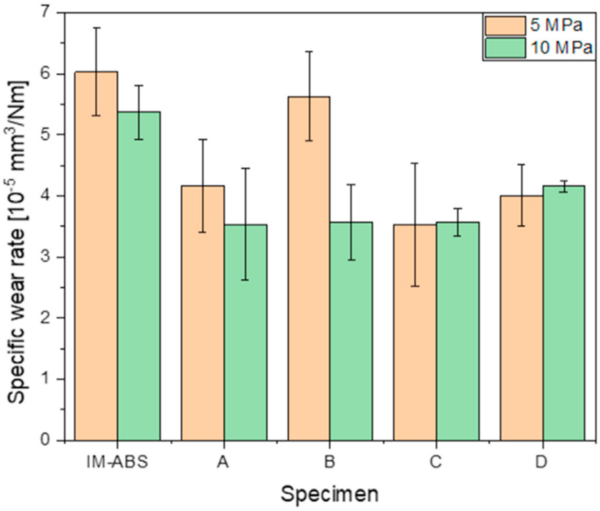

Fig. 18 – **Specific wear rates at 80 N and 160 N for injection molded (IM-ABS) and 3D printed ABS (A: 0°/90° raster angle, 20 mm/s printing speed; B: 0°/90° raster angle, 50 mm/s printing speed; C: +45°/-45° raster angle, 20 mm/s printing speed; D: +45°/-45° raster angle, 50 mm/s printing speed).**

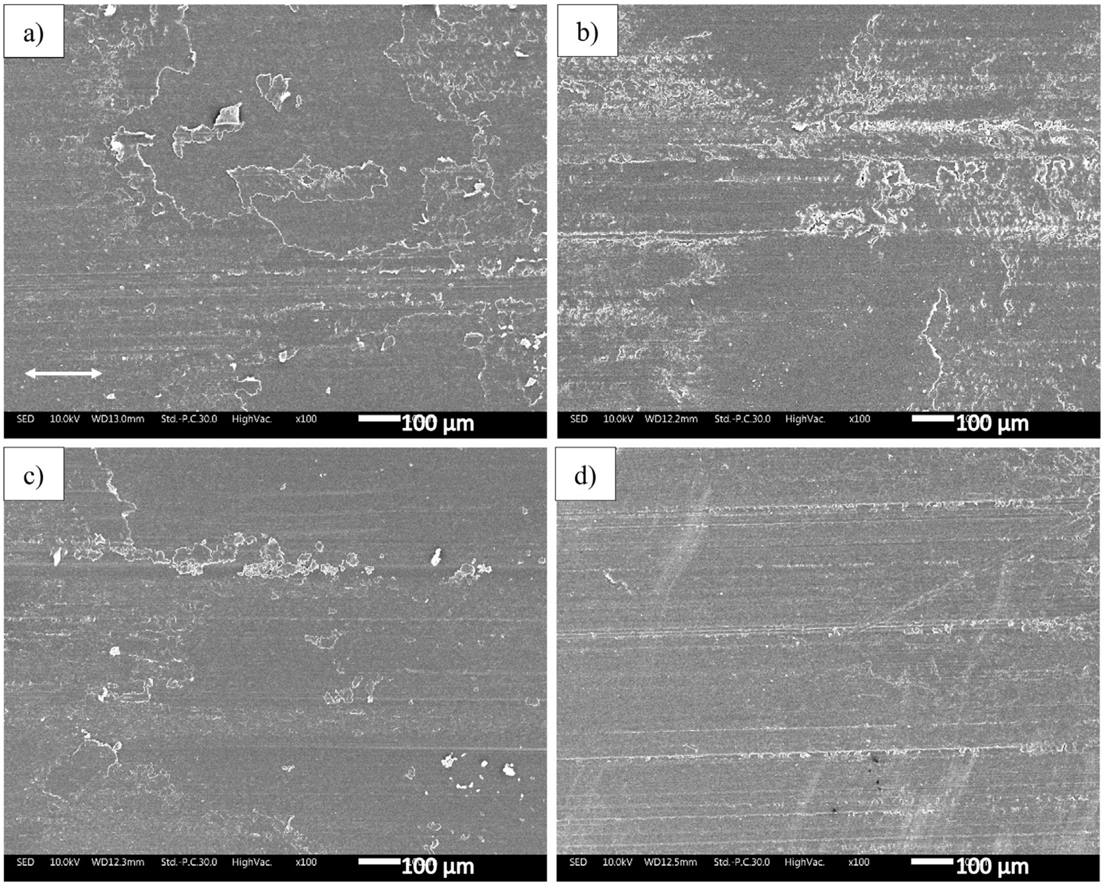

Fig. 19 – Worn surfaces of 3D printed ABS, pin-on-plate under 5 MPa contact pressure, 0.02 m/s sliding speed: (a) 0°/90° raster angle, 20 mm/s printing speed; (b) 0°/90° raster angle, 50 mm/s printing speed; (c) +45°/-45° raster angle, 20 mm/s printing speed; (d) +45°/-45° raster angle, 50 mm/s printing speed.

whilst achieving comparable frictional behavior resulting in lower printing time.

Furthermore, friction coefficients of 3D printed ABS parts are compared with conventionally manufactured commercial ABS. The injection-molded ABS from Ensinger plastics – TECARAN ABS [32] showed average friction coefficients of around 0.3–0.4. The recorded friction coefficients in this study for conventional ABS agree with the earlier reported values in the literature for ABS-steel friction pairs [52,53]. 3D-ABS exhibited 25%–40% reduced friction coefficients compared to IM-ABS. This observation suggests that 3D printing of polymers could potentially improve the frictional properties of tribological components compared to conventional methods. 3D printing produced parts with higher roughness parameters resulting in higher asperity peaks in contact. This provides a smaller initial contact area and higher initial contact pressure resulting in relatively faster smoothening of asperities. Friction tends to be lower at a lower sliding speed after the removal of initial surface asperities by abrasion during dry sliding. Sedlaček et al. [54] reported similar phenomena with Al_2O_3 balls on contact with 100Cr6 steel samples of varying roughness parameters, suggesting that friction tends to be lower with higher roughness under dry sliding at low speeds. Therefore, 3D-printed rough polymer parts could potentially improve compliance with steel surfaces in contact. Nonetheless, further detailed investigation and comparison need to be carried out on the tribological behavior of FFF 3D printed versus conventionally manufactured parts to establish a firm correlation.

3.6.3. *Specific wear rate (SWR)*

Fig. 18 represents the specific wear rates of printed ABS with varying printing speeds and raster angles. Process parameter variables in this study had a minor influence on the wear behavior of printed ABS. However, the pre-existing internal defects and increased surface roughness at higher printing speeds affected the wear behavior. The specimens printed with 50 mm/s printing speed (B and D) showed relatively higher wear rates when compared to 20 mm/s printing speed (A and C) for both raster angles. Higher surface roughness specimens at higher printing speeds exhibiting increased wear rates are in agreement with the observations from Norani et al. [28] and Amiruddin et al. [55]. The influence of increased printing speed in this study is notably higher for 0°/90° specimens with larger standard deviations. On the other hand, increased applied normal loads reduced the specific wear rates of 0°/90° specimens (A and B), $p = 0.015 < 0.05$ (statistically significant differences), while +45°/-45° specimens (C and D) showed an insignificant variation in the specific wear rates with increased loads, $p = 0.778 > 0.05$

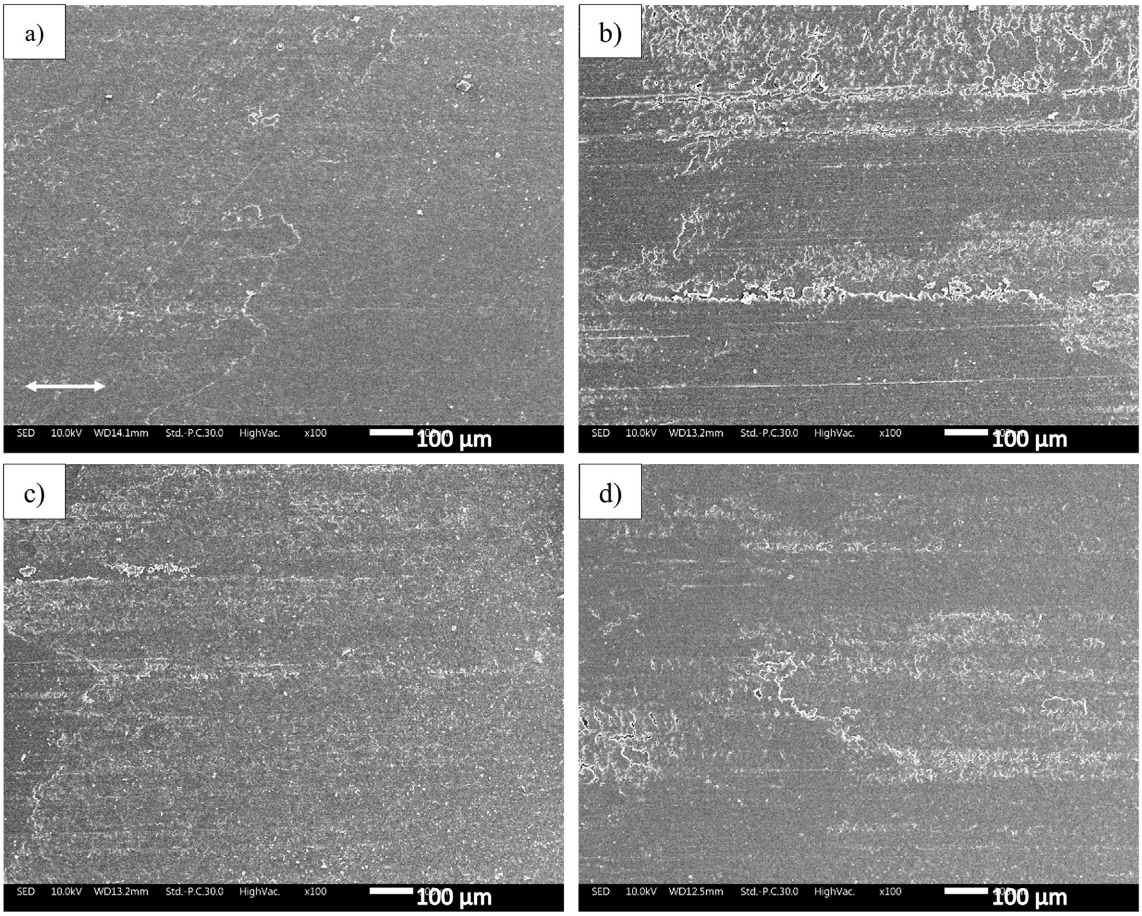

Fig. 20 – **Worn surfaces of 3D printed ABS, pin-on-plate under 10 MPa contact pressure, 0.02 m/s sliding speed: (a) 0°/90° raster angle, 20 mm/s printing speed; (b) 0°/90° raster angle, 50 mm/s printing speed; (c) +45°/-45° raster angle, 20 mm/s printing speed; (d) +45°/-45° raster angle, 50 mm/s printing speed.**

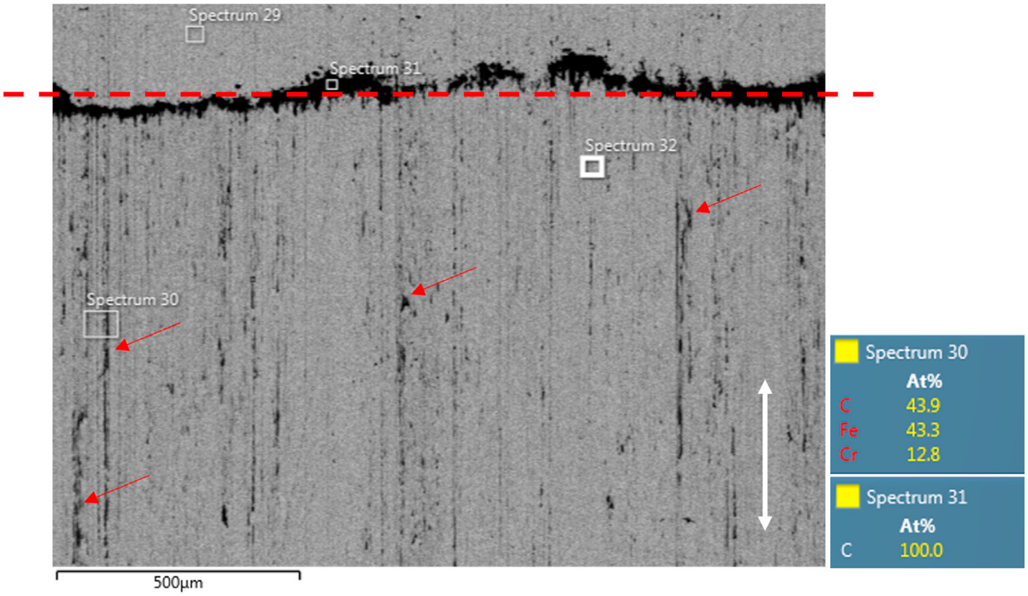

Fig. 21 – **SS countersurface after tribological test with 3D printed ABS component (Specimen D: +45°/-45° raster angle, 50 mm/s printing speed).**

(statistically insignificant differences), presented in the Supporting information (Figs. S9 and S10). It indicates that +45°/-45° raster angle orientation produces parts yielding better wear performance under varying loading conditions compared to 0°/90° raster angles. Specific wear rates observed in this study for printed ABS are one order lower than recent findings [28], where FFF printed ABS showed specific wear rates in the order of 10^{-4} mm^3/Nm. The testing conditions of that study were 39.24 N load and 600 rpm sliding speed resulting in 800 m of total sliding distance with a pin-on-disc configuration. The observed differences could be ascribed to the varying tribological testing conditions compared to this study. Although, the discrepancies in the wear behavior of printed ABS should be noted.

FFF printed parts were compared with the injection-molded ABS for wear behavior analysis. Traditionally, layer-on-layer fabrication in 3D printing produced parts with higher void contents and lower compactness [56] and was susceptible to higher sliding wear compared to injection molding. Interestingly, printed ABS in this study exhibited the desirable effect of improved specific wear rates at the same order (10^{-5} mm^3/Nm) as injection molded parts. The explanation for this could be due to the improved microstructure properties and interlayer bonding of parts printed with a heated build chamber. On the other hand, ABS compositions with varying butadiene content can influence the wear rate and friction coefficient of printed ABS components [31,57]. Thereby, the variation in wear rates could have resulted from different processing conditions and base material composition employed in the two methods.

3.6.4. *Wear mechanisms*

SEM images of worn surfaces of wear-tested pins under 5 and 10 MPa contact pressures are presented in Figs. 19 and 20, respectively. The sliding direction of polymer pins over the countersurface is indicated by the white arrow. Abrasion was observed as the predominant wear mechanism for printed ABS from SEM analysis. The rough asperities on the pin contact face led to deformation during sliding and as material removal begins, shallow grooves start to form on the pin surface. With repeated sliding, adjacent beads separate from each other, and materials on the individual layers peel off due to subsurface cracking resulting from plastic deformation. The pre-existing voids act as initiators for crack growth and propagation, consequently accelerating the wear process on the individual layers. Thereby, internal defects and surface irregularities of the printed ABS highly influenced the wear behavior, exhibiting higher content of material removal and delamination for higher printing speed. The formation of grooves is also more prominent for specimens fabricated with higher printing speed and under 5 MPa contact pressure compared to 10 MPa, as seen in Fig. 19(b, d). The sliding surfaces worn under 10 MPa contact pressure are comparatively smoother than 5 MPa for all specimens, see Figs. 19 and 20.

The wear particles observed in Fig. 19(a and b) are reflective of the higher wear rates for 0°/90° specimens (A and B) under 5 MPa contact pressure observed in section 3.6.3. The abrasive flakes and debris present on the worn pin surfaces indicate the lower resistance of the corresponding material. For 0°/90° specimens under both contact pressures, worn surfaces of the specimen with higher printing speed show higher content of wear debris, Fig. 19(a and b) and Fig. 20(a and b). This suggests that increased printing speed resulting in higher surface roughness influenced the wear behavior of 0°/90° specimens. The worn surfaces of all +45°/-45° (C and D) specimens, on the other hand, show similar wear behavior under 10 MPa, whilst few grooves on the sliding surface were observed under 5 MPa contact pressure, see Fig. 19(c and d) and Fig. 20(c and d). This indicates that raster angle orientation has a higher influence on the wear behavior of printed materials, with +45°/-45° specimens exhibiting relatively higher resistance to sliding wear compared to 0°/90° specimens in this study.

The counter surfaces after tribological testing were inspected for transfer film formation of printed ABS on SS plates. All printed ABS specimens exhibited discontinuous patchy transfer films deposited on the plates, regardless of varying raster angles, printing speeds, and applied loads. Analysis of the countersurface after dry sliding of specimen D at 20 mm/s speed under 10 MPa contact pressure is presented in Fig. 21. The dark regions in the wear track denoted with red arrows represent the patchy polymer transfer films along the pin sliding direction (white arrow). EDX confirmed the carbon element indicative of polymer patches deposited on the plates, for instance, spectrum 30. In addition, it was observed that wear track edges contained polymer wear debris accumulated from the continuous reciprocating sliding. EDX at the wear track edge (spectrum 31) confirmed the carbon-based deposit along the upper edge of the wear track, indicated by the red dashed line in Fig. 21.

3.7. *Influence of processing conditions on printing time*

The influence of varying raster angle orientations and printing speeds on the total build time of testing parts was also studied. The printing time of test specimens greatly varied for two opted printing speeds in this study. The total time to fabricate a batch of two tensile testing specimens at 20 mm/s printing speed was 3 h and 36 min for both raster angles, while the same took 1 h 30 min at 50 mm/s. Similarly, the printing time for a batch of 6 flexural testing specimens at 20 mm/s speed was 6 h 52 min, while increasing the printing speed to 50 mm/s took 2 h 51 min. The reduction in printing time without adversely compromising the material properties is a positive outcome. Importantly, performance variation for the parts printed with higher speed inside the heated chamber is greatly reduced compared to the open systems in the literature. In general, open-system printers that print at higher speeds produce parts with inferior properties [8,17–19]. However, in this study, the closed system fabrication approach at increased printing speed yielded ABS parts exhibiting comparable performance with a significantly reduced printing time.

Although in the early stages, works done on large-format high-speed FFF 3D printing by industries like BigRep [58] and Thermwood [59] as well as researchers from Oak Ridge National Laboratory [60,61] suggest faster and more economical solutions for producing large industrial components. Similarly, in-process direct annealing systems, topology optimization, and automated post-processing as alternative solutions to reduce processing defects are also being studied. Researchers have been looking into embedded sensors and machine learning to enable smarter 3D printing for improved surface finish, increased efficiency, and repeatability via in-process monitoring to reduce built time [62].

4. Conclusions

This study aimed to understand the formation and distribution of defects arising from material extrusion-based FFF 3D printing. Mechanical and tribological tests were carried out to investigate the influence of processing-induced defects on the printed part characteristics. Microstructure and surface analysis were performed using WLI, SEM, and XMT scans. The observations of this study provide an understanding of the interdependency of material characteristics with the processing conditions. The major findings of this investigation can be concluded as follows.

- Porosity analysis from XMT scans showed the formation and distribution of internal defects. Pores are mainly distributed along the raster angle orientation throughout the specimen, +45°/-45° raster angles yielding lower content of micropores between the material infill.
- Microscopic analysis of fractured surfaces revealed a mixed mode of fracture mechanism. 0°/90° raster angle orientation primarily showed a brittle fracture, while the ductile mode was predominant with +45°/-45° raster angles.
- Raster angle orientation influences the mechanical properties and tribological performance. Printing with +45°/-45° raster angles yielded optimal mechanical properties with more than 60% increased elongation at break exhibiting improved resistance to wear.
- Roughness and texture of the contact surface impact the friction and wear behavior of printed parts, with higher asperity peaks leading to delayed running-in during sliding.
- Increased printing speed showed an insignificant variation in the steady-state frictional behavior of printed polymers. Friction behavior is mainly dependent on the raster angle orientation and applied normal loads.
- FFF-printed ABS exhibited up to 40% friction reduction compared to commercial injection-molded ABS, while the specific wear rates were recorded in the same order of magnitude (10^{-5} mm^3/Nm) for both processing methods.
- Increased printing speed allowed up to 58% effective reduction in printing time for testing parts with comparable properties.

This study provides new information about the correlation between internal porosity and surface defects on the tribology of printed parts. Fabrication of parts without a significant trade-off of tribological and mechanical properties was achieved at increased printing speeds. It enables the possibility of time-efficient and cost-effective investigations on the 3D printable polymers for load-bearing applications. This is a step toward sustainable manufacturing via polymer 3D printing with a great potential of minimizing energy consumption. All in all, the future of polymer 3D printing holds a huge potential to provide significant enhancement to the current manufacturing capabilities.

Credit authorship contribution statement

Nayan Dhakal: Conceptualization, Methodology, Investigation, Data curation, Formal analysis, Visualization, Writing – Original Draft. **Xiaolong Wang**: Conceptualization, Resources. **Cayetano Espejo**: Supervision, Writing – Review & Editing. **Ardian Morina**: Supervision, Writing – Review & Editing. **Nazanin Emami**: Conceptualization, Methodology, Supervision, Writing – Review & Editing, Resources, Funding acquisition.

Declaration of competing interest

The authors declare that they have no known competing financial interests or personal relationships that could have appeared to influence the work reported in this paper.

Acknowledgements

The authors would like to thank the European Union's Horizon 2020 research and innovation programme for funding this research under the GreenTRIBOS, Marie Skłodowska-Curie grant agreement No. 860246.

Appendix A. Supplementary data

Supplementary data to this article can be found online at https://doi.org/10.1016/j.jmrt.2023.01.086.

Supporting information

Supplementary data associated with this article can be found in the online version.

REFERENCES

[1] Gebler M, Schoot Uiterkamp AJM, Visser C. A global sustainability perspective on 3D printing technologies. Energy Pol 2014;74:158–67. https://doi.org/10.1016/j.enpol.2014.08.033.
[2] Khajavi SH, Partanen J, Holmström J. Additive manufacturing in the spare parts supply chain. Comput Ind 2014;65(1):50–63. https://doi.org/10.1016/j.compind.2013.07.008.
[3] Mani M, Lyons KW, Gupta SK. Sustainability characterization for additive manufacturing. J Res Natl Inst Stand Technol 2014;119:419–28. https://doi.org/10.6028/jres.119.016.
[4] Valino AD, Dizon JRC, Espera AH, Chen Q, Messman J, Advincula RC. Advances in 3D printing of thermoplastic polymer composites and nanocomposites. Prog Polym Sci 2019;98. https://doi.org/10.1016/j.progpolymsci.2019.101162.
[5] Campbell TA, Ivanova OS. 3D printing of multifunctional nanocomposites. Nano Today 2013;8(2):119–20. https://doi.org/10.1016/j.nantod.2012.12.002.
[6] Dey A, Yodo N. A systematic survey of FDM process parameter optimization and their influence on Part Characteristics. J Manufac Mate Process 2019;3(3). https://doi.org/10.3390/jmmp3030064.

[7] Akande SO. Dimensional accuracy and surface finish optimization of fused deposition modelling parts using desirability function analysis. Int J Eng Res Technol 2015;(4):196–202. https://doi.org/10.17577/IJERTV4IS040393.

[8] Popescu D, Zapciu A, Amza C, Baciu F, Marinescu R. FDM process parameters influence over the mechanical properties of polymer specimens: a review. Polym Test 2018;69:157–66. https://doi.org/10.1016/j.polymertesting.2018.05.020.

[9] Mohamed OA, Masood SH, Bhowmik JL. Analysis of wear behavior of additively manufactured PC-ABS parts. Mater Lett 2018;230:261–5. https://doi.org/10.1016/j.matlet.2018.07.139.

[10] Keshavamurthy R, Tambrallimath V, Rajhi AA, R MS, Patil AY, Yunus Khan TM, et al. Influence of solid lubricant addition on friction and wear response of 3D printed polymer composites. Polymers 2021;13(17). https://doi.org/10.3390/polym13172905.

[11] Brackett J, Cauthen D, Condon J, Smith T, Gallego N, Kunc V, et al. The impact of infill percentage and layer height in small-scale material extrusion on porosity and tensile properties. Addit Manuf 2022;58. https://doi.org/10.1016/j.addma.2022.103063.

[12] Ahn SH, Montero M, Odell D, Roundy S, Wright PK. Anisotropic material properties of fused deposition modeling ABS. Rapid Prototyp J 2002;8(4):248–57. https://doi.org/10.1108/13552540210441166.

[13] Tymrak BM, Kreiger M, Pearce JM. Mechanical properties of components fabricated with open-source 3-D printers under realistic environmental conditions. Mater Des 2014;58:242–6. https://doi.org/10.1016/j.matdes.2014.02.038.

[14] Gordelier TJ, Thies PR, Turner L, Johanning L. Optimising the FDM additive manufacturing process to achieve maximum tensile strength: a state-of-the-art review. Rapid Prototyp J 2019;25(6):953–71. https://doi.org/10.1108/rpj-07-2018-0183.

[15] Buj-Corral I, Bagheri A, Sivatte-Adroer M. Effect of printing parameters on dimensional error, surface roughness and porosity of FFF printed parts with grid structure. Polymers 2021;13(8). https://doi.org/10.3390/polym13081213.

[16] Krolczyk G, Raos P, Legutko S. Experimental analysis of surface roughness and surface texture of machined and fused deposition modelled parts. Tehnicki Vjesnik-Technical Gazette 2014;21(1):217–21.

[17] Peterson AM. Review of acrylonitrile butadiene styrene in fused filament fabrication: a plastics engineering-focused perspective. Addit Manuf 2019;27:363–71. https://doi.org/10.1016/j.addma.2019.03.030.

[18] Wang P, Zou B, Xiao H, Ding S, Huang C. Effects of printing parameters of fused deposition modeling on mechanical properties, surface quality, and microstructure of PEEK. J Mater Process Technol 2019;271:62–74. https://doi.org/10.1016/j.jmatprotec.2019.03.016.

[19] Wang P, Zou B, Ding S, Li L, Huang C. Effects of FDM-3D printing parameters on mechanical properties and microstructure of CF/PEEK and GF/PEEK. Chin J Aeronaut 2021;34(9):236–46. https://doi.org/10.1016/j.cja.2020.05.040.

[20] Wang F, Luo F, Huang Y, Cao X, Yuan C. 4D printing via multispeed fused deposition modeling. Adv Mater Tech 2022. https://doi.org/10.1002/admt.202201383.

[21] Nomani J, Wilson D, Paulino M, Mohammed MI. Effect of layer thickness and cross-section geometry on the tensile and compression properties of 3D printed ABS. Mater Today Commun 2020;22. https://doi.org/10.1016/j.mtcomm.2019.100626.

[22] Vicente CMS, Martins TS, Leite M, Ribeiro A, Reis L. Influence of fused deposition modeling parameters on the mechanical properties of ABS parts. Polym Adv Technol 2019;31(3):501–7. https://doi.org/10.1002/pat.4787.

[23] Rankouhi B, Javadpour S, Delfanian F, Letcher T. Failure analysis and mechanical characterization of 3D printed ABS with respect to layer thickness and orientation. J Fail Anal Prev 2016;16(3):467–81. https://doi.org/10.1007/s11668-016-0113-2.

[24] Ertan R, Durgun I. Experimental investigation of FDM process for improvement of mechanical properties and production cost. Rapid Prototyp J 2014;20(3):228–35. https://doi.org/10.1108/rpj-10-2012-0091.

[25] Torrado AR, Roberson DA. Failure analysis and anisotropy evaluation of 3D-printed tensile test specimens of different geometries and print raster patterns. J Fail Anal Prev 2016;16(1):154–64. https://doi.org/10.1007/s11668-016-0067-4.

[26] Riddick JC, Haile MA, Wahlde RV, Cole DP, Bamiduro O, Johnson TE. Fractographic analysis of tensile failure of acrylonitrile-butadiene-styrene fabricated by fused deposition modeling. Addit Manuf 2016;11:49–59. https://doi.org/10.1016/j.addma.2016.03.007.

[27] Kaur G, Singari RM, Kumar H. A review of fused filament fabrication (FFF): process parameters and their impact on the tribological behavior of polymers (ABS). Mater Today Proc 2022;51:854–60. https://doi.org/10.1016/j.matpr.2021.06.274.

[28] Norani MNM, Abdollah MFB, Abdullah MIHC, Amiruddin H, Ramli FR, Tamaldin N. 3D printing parameters of acrylonitrile butadiene styrene polymer for friction and wear analysis using response surface methodology. Proc IME J J Eng Tribol 2020;235(2):468–77. https://doi.org/10.1177/1350650120925601.

[29] Norani MNM, Abdullah MIHC, Abdollah MFB, Amiruddin H, Ramli FR, Tamaldin N. Tribological analysis of a 3D-printed internal triangular flip ABS pin during running-in stage. J Tribologi 2020;27:42–56.

[30] Prusinowski A, Kaczynski R. Tribological behaviour of additively manufactured fiber-reinforced thermoplastic composites in various environments. Polymers 2020;12(7). https://doi.org/10.3390/polym12071551.

[31] Bankupalli N, Srinivasa Rao D, Vamsi Krishna TS. Effect of process parameters and butadiene content on friction and wear behaviour of ABS components. Mater Today Proc 2021;41:416–21. https://doi.org/10.1016/j.matpr.2020.09.808.

[32] Ensinger. TECARAN ABS grey. [cited 2021 August 10]; Available from: https://www.ensingerplastics.com/en/shapes/products/tecaran-abs-grey.

[33] ASTM. D638 - standard test method for tensile properties of plastics. ASTM; 2014.

[34] ASTM. D790 - standard test methods for flexural properties of unreinforced and reinforced plastics and electrical insulating materials. ASTM; 2017.

[35] ASTM. D792 - standard test methods for density and specific gravity (relative density) of plastics by displacement. ASTM; 2020.

[36] ASTM. D2734 - standard test methods for void content of reinforced plastics. ASTM; 2016.

[37] JF R, JP T, JE R. Mechanical behavior of acrylonitrile butadiene styrene (ABS) fused deposition materials. Experimental investigation. Rapid Prototyp J 2001;7(3):148–58. https://doi.org/10.1108/13552540110395547.

[38] Saenz F, Otarola C, Valladares K, Rojas J. Influence of 3D printing settings on mechanical properties of ABS at room temperature and 77 K. Add Manufac 2021;39. https://doi.org/10.1016/j.addma.2021.101841.

[39] Wu W, Geng P, Li G, Zhao D, Zhang H, Zhao J. Influence of layer thickness and raster angle on the mechanical properties of 3D-printed PEEK and a comparative mechanical

study between PEEK and ABS. Materials 2015;8(9):5834–46. https://doi.org/10.3390/ma8095271.

[40] Torrado Perez AR, Roberson DA, Wicker RB. Fracture surface analysis of 3D-printed tensile specimens of novel ABS-based materials. J Fail Anal Prev 2014;14(3):343–53. https://doi.org/10.1007/s11668-014-9803-9.

[41] Meng S, He H, Jia Y, Yu P, Huang B, Chen J. Effect of nanoparticles on the mechanical properties of acrylonitrile-butadiene-styrene specimens fabricated by fused deposition modeling. J Appl Polym Sci 2017;134(7). https://doi.org/10.1002/app.44470.

[42] Oropallo W, Piegl LA. Ten challenges in 3D printing. Eng Comput 2015;32(1):135–48. https://doi.org/10.1007/s00366-015-0407-0.

[43] Wickramasinghe S, Do T, Tran P. FDM-based 3D printing of polymer and associated composite: a review on mechanical properties, defects and treatments. Polymers 2020;12(7). https://doi.org/10.3390/polym12071529.

[44] Khosravani MR, Schuurmann J, Berto F, Reinicke T. On the post-processing of 3D-printed ABS parts. Polymers 2021;13(10). https://doi.org/10.3390/polym13101559.

[45] Neff C, Trapuzzano M, Crane NB. Impact of vapor polishing on surface roughness and mechanical properties for 3D printed ABS. In: Proceedings of the solid freeform fabrication symposium – an additive manufacturing conference. Austin, TX, USA: The university of Texas; 2016. p. 2295–304.

[46] Braun K, Willenborg E, Schleifenbaum JH. Laser polishing as a new post process for 3D-printed polymer parts. In: 11th CIRP Conference on Photonic Technologies; 2020. p. 134–8. https://doi.org/10.1016/j.procir.2020.09.026.

[47] Yang H, Ji F, Li Z, Tao S. Preparation of hydrophobic surface on PLA and ABS by fused deposition modeling. Polymers 2020;12(7). https://doi.org/10.3390/polym12071539.

[48] Alsoufi MS, Elsayed AE. Surface roughness quality and dimensional accuracy—a comprehensive analysis of 100% infill printed parts fabricated by a personal/desktop cost-effective FDM 3D printer. Mater Sci Appl 2018;9(1):11–40. https://doi.org/10.4236/msa.2018.91002.

[49] Campbell RI, Martorelli M, Lee HS. Surface roughness visualisation for rapid prototyping models. Comput Aided Des 2002;34:717–25. https://doi.org/10.1016/S0010-4485(01)00201-9.

[50] Józwik J, Ostrowski D, Milczarczyk R, Krolczyk GM. Analysis of relation between the 3D printer laser beam power and the surface morphology properties in Ti-6Al-4V titanium alloy parts. J Braz Soc Mech Sci Eng 2018;40(4). https://doi.org/10.1007/s40430-018-1144-2.

[51] Quaglini V, Dubini P. Friction of polymers sliding on smooth surfaces. Adv Tribol 2011;2011:1–8. https://doi.org/10.1155/2011/178943.

[52] Ben Difallah B, Kharrat M, Dammak M, Monteil G. Mechanical and tribological response of ABS polymer matrix filled with graphite powder. Mater Des 2012;34:782–7. https://doi.org/10.1016/j.matdes.2011.07.001.

[53] Rojsatean J, Larpsuriyakul P, Prakymoramas N, Thanomjitr D, Kaewket S, Singsom T, et al. Friction characteristics of self-lubricating ABS under different surface roughnesses and temperatures. Tribol Int 2017;109:229–37. https://doi.org/10.1016/j.triboint.2016.12.055.

[54] Sedlaček M, Podgornik B, Vižintin J. Influence of surface preparation on roughness parameters, friction and wear. Wear 2009;266(3–4):482–7. https://doi.org/10.1016/j.wear.2008.04.017.

[55] Amiruddin H, Abdollah MFB, Norashid NA. Comparative study of the tribological behaviour of 3D-printed and moulded ABS under lubricated condition. Mater Res Express 2019;6(8). https://doi.org/10.1088/2053-1591/ab2152.

[56] Rodriguez JF, J PT, Renaud JE. Characterization of the mesostructure of fused-deposition acrylonitrile-butadiene-styrene materials. Rapid Prototyp J 2000;6(3):175–85. https://doi.org/10.1108/13552540010337056.

[57] Bankupalli N, Srinivasa Rao D, Vamsi Krishna TS. Role of butadiene content on tribological properties of polymeric components fabricated by FDM. Mater Today Proc 2021;38:3019–26. https://doi.org/10.1016/j.matpr.2020.09.325.

[58] BigRep. BigRep introduces A new generation of large-format 3D printers tailored to their users' applications. 2021 [cited 2022 November 20]; Available from: https://bigrep.com/posts/new-generation-large-3d-printers/.

[59] Thermwood Lsam - Large Scale Additive Manufacturing. [cited 2022 November 20]; Available from: https://www.thermwood.com/lsam_home.htm.

[60] Chesser P, Love L, Witt A, Roos P. Feasibility of using additive manufacturing to produce axial flow hydropower turbine housing, runner, and draft tube. In: Energy UDO, editor. Oak Ridge, Tennessee: Oak Ridge National Laboratory; 2021.

[61] Billah KMM, Heineman J, Mhatre P, Roschli A, Post B, Kumar V, et al. Large-scale additive manufacturing of self-heating molds. Addit Manuf 2021;47. https://doi.org/10.1016/j.addma.2021.102282.

[62] Moretti M, Bianchi F, Senin N. Towards the development of a smart fused filament fabrication system using multi-sensor data fusion for in-process monitoring. Rapid Prototyp J 2020;26(7):1249–61. https://doi.org/10.1108/rpj-06-2019-0167.